energies

MDPI

Article

Numerical Study on the Performance of a Gravitational Water Vortex Hydro-Turbine System with a Cylindrical Basin

Nosare Maika, Mehdi Khatamifar and Wenxian Lin *

College of Science and Engineering, James Cook University, Townsville, QLD 4811, Australia; nosare.maika@my.jcu.edu.au (N.M.); mehdi.khatamifar2@jcu.edu.au (M.K.)
* Correspondence: wenxian.lin@jcu.edu.au

Abstract

Gravitational water vortex power systems are one of the cost-effective systems of extracting low head hydro power. This study investigates numerically a gravitational water vortex power system five-blade turbine rotating in a cylindrical basin for three blade shapes (flat, curved, and vertical twist) and three diameters of the discharge orifice at the basin bottom. The numerical simulations adopted a scaled down model using the Froude number similarity and employed the Volume of Fluid, Moving Reference Frame, and SST $k-\omega$ turbulence model. The system performance was examined both qualitatively and quantitatively for five turbine rotation speeds over 40–120 revolution/minute (RPM). It was found that blade shape, orifice diameter, and turbine rotation speed have significant effects on system performance. For a specific blade shape and discharge orifice diameter combination, the generated torque and power increases almost linearly at a large rate when the turbine rotation speed is increased from 40 RPM to 80 RPM and then decreases, also essentially linearly, at a much smaller rate from 80 RPM to 120 RPM. The optimal rotation speed was found to be 80 RPM across the speeds considered for all cases. It was also shown that the system with an intermediate diameter ratio performs better for each blade shape and the system with the curved blades performs better than the other two blade shapes. The results further show that for the cases considered, the most favorable operating condition was achieved by using a combination of a five-bladed curved turbine, a medium discharge orifice diameter ($d_o/D \approx 0.16$) in a cylindrical basin, and a rotational speed of 80 RPM, yielding relatively the highest efficiency of up to 62%, which are very good outcomes for such low head hydropower systems.

Keywords: gravitational water vortex hydro turbine system; torque; hydropower generation; cylindrical basin; turbine blade; turbulent kinetic energy

Academic Editor: Mario Marchesoni

Received: 24 December 2025
Revised: 24 February 2026
Accepted: 4 March 2026
Published: 6 March 2026

1. Introduction

The use of electrical energy is an integral part of the modern way of life. However, not everyone has access to it, with only 13% of the world's population having access to electricity. Extracting energy in a hydro dynamic environment has long been widely used due to its sustainable nature of energy source and has become even more important to reach net zero emissions by 2050. According to the International Hydropower Association [1], the total global hydropower installed capacity in 2023 was 1416 GW (Giga-Watts), and 4185 TWh (Terawatt-hours) electricity generated from hydropower.

Large-scale hydropower systems have been major contributors to the global hydropower capacity but they have serious impacts on the ecosystem. Energy from small

hydropower systems (up to 10 MW—Mega-Watts) is considered as a key contributor to the overall energy development, especially in the developing world. Small hydropower systems had a worldwide power capacity of 79 GW in 2022 [2]. Efforts are increasing to invest in smaller hydropower systems to improve the scope of power generation and distribution and to increase renewable energy sources. One such smaller hydropower systems is a gravitational water vortex hydro-turbine system (GWVHT), which is also one of the most convenient, compact, and cheap hydropower systems particularly favored in remote, rural, and mountainous areas where the demand is on a very small scale and an electric grid is not readily available.

A GWVHT system is an ultra-low-head micro-hydropower system operating in the range of 0.7 m–2 m head without the need of a large reservoir and installation area. It is considered to be a sustainable and green technology due to its low head and direct water installations and is still considered to be a relatively new technology. As sketched in Figure 1, a typical GWVHT system consists of an inlet water channel (passage), an outlet water channel (passage), a circular basin with an opening (usually an orifice) on its bottom for the discharge of water in the basin to the outlet channel, and a turbine with multiple blades and a vertical shaft connected to the electricity generator [3,4]. Water from natural streams like rivers, creeks, mountains, or coastal currents is channelled into the inlet channel to enter the basin at the top and is discharged through the discharge orifice into the outlet channel. The natural flow of water through the system creates a free surface vortex caused by the Coriolis force and the vorticity increases towards the orifice, which also increases the water circulation, resulting in the pressure to fall below atmospheric pressure, which leads to an air core, with the radius of the air core decreasing towards the orifice [5]. The free flow of the vortex energy is converted into mechanical energy by the turbine blades and then into electric energy by the generator connected to the turbine through the shaft. Since it has a very small head difference, it works by the dynamic forces generated by the vortex rather than the pressure head difference [6]. The performance of a GWVHT system can be easily assessed by the power output produced and by its efficiency.

In the landscape of ultra-low-head ($H < 3.0$ m) hydropower, gravitational water vortex hydro-turbines (GWVHT) have emerged as a robust alternative to conventional axial and cross-flow architectures, particularly for decentralized and off-grid applications [7]. While axial turbines, such as the Kaplan design, can exceed 90% efficiency at large scale under optimized conditions, they require complex civil works and remain economically prohibitive for pico-scale installations [8]. Recent studies have shown that modern cross-flow turbines (CFTs) can achieve efficiencies between 70 and 90% under low head conditions of 0.5–5 m through optimized blade design, pressurized intake systems, and improved flow control [9–12]. A CFT operates on a pressure–velocity-driven mechanism, where water is accelerated through nozzles and diverted tangentially to the blades, with the resulting impulse and reactive forces transferring momentum to the blades for power generation. All these require enclosed channels, a nozzle mechanism, and controlled pressure conditions for a CFT to operate efficiently. To ensure that a CFT provides stable high performance in controlled channels, installation in open or remote environments can be costly and complex.

Recent advancements highlight the unique capability of GWVHT systems to exploit the free-surface vortex phenomenon, offering enhanced fish-friendliness and debris tolerance, with experimental efficiencies reaching up to 60.85% through optimized spiral inlet configurations [8]. However, their performance is highly sensitive to air core stability and the hydrodynamic interaction between the runner and the vortex structure [13]. In particular, the conversion of the hydraulic head into tangential kinetic energy is strongly governed by basin geometry; for example, conical configurations with a 45° deviation angle have been shown to maximize tangential velocities [14]. This sensitivity necessitates

rigorous high-fidelity computational fluid dynamics (CFD) and Response Surface Methodology (RSM) to mitigate turbulence-induced losses and optimize energy extraction [15]. A practical limitation of GWVHT and other ultra-low-head turbines is their inherently low rotational speed, which is often well below the optimal operating speed of conventional electrical generators. This mismatch typically necessitates mechanical speed increasers or specially designed low-speed generators, both of which introduce additional losses and system complexity. Recent studies on low-speed generator design, particularly axial-flux permanent magnet machines, demonstrate that direct-drive configurations can effectively generate electrical power at low rotational speeds without gearboxes, thereby reducing conversion losses and improving overall system reliability [16]. For example,the test cases of 40–120 RPM are evaluated to compare with the generator compatibility rather than turbine alone. This is to ensure that the turbine torque at each RPM meets the electromagnetic demand of the available permanent magnet generator (PMG) whilst maintaining stable vortex structure and avoiding excessive flow blockages. GWVT achieve high efficiency not from high speed but from momentum exchange and pressure distribution, thus allowing power extraction at low angular velocity. This makes GWVT technically viable for remote application. Thus, low-speed, high-torque direct-drive PMG system with power electronics are the most appropriate generation solution for GWVT systems [17].

Even though a GWVHT has a vertical shaft, it is not equivalent to a conventional vertical axis turbine (VAT). The energy extraction methods differ fundamentally. In MRF-VOF simulations, torque is extracted from pressure gradient in vortex flow and not from uniform approach velocity as in a normal VAT system. It uses very low head and low discharge rates to extract energy efficiently where the conventional reaction turbines are unable to do. Water quality is a critical factor in any hydropower system. Solid load in the incoming water resource for the GWVT system is to be controlled using a relevant mechanism. Since GWVT operates with a free surface vortex and slow rotational speed, excessive sediment can significantly affect the hydraulic performance and reduce mechanical reliability [18].

GWVHT systems are still in the developing stage, with reported efficiencies ranging widely from about 17% to 85% [4], indicating significant potential for performance improvement and optimization.

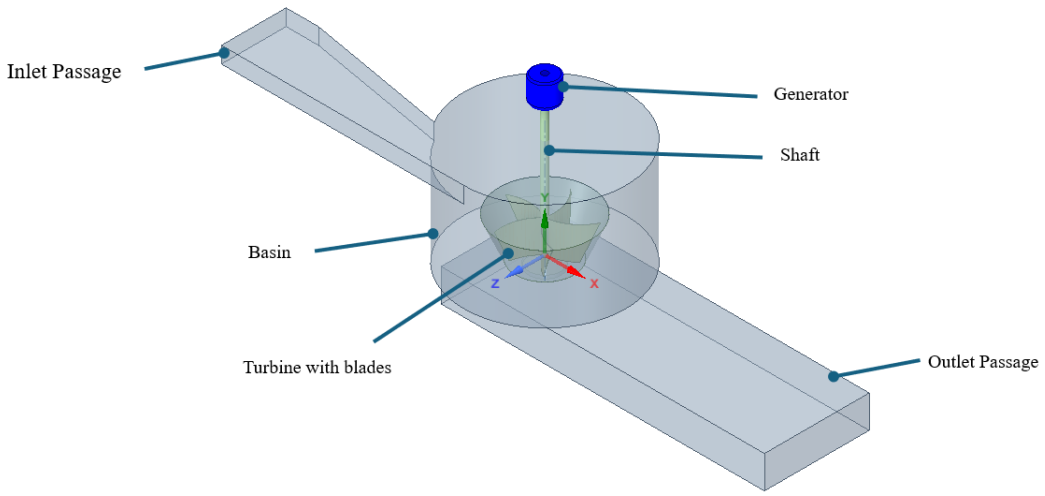

Figure 1. Schematic of a typical GWVHT system with a shallow cylindrical basin and its main components.

As reviewed by some researchers (e.g., [4,19–21]) and more recently by the present authors [7], there have been many previous studies on GWVHT systems. Most of the past studies were conducted to improve and optimize the parametric and operational features of GWVHT systems using analytical and experimental methods. More recently, the numerical

method using computational fluid dynamics (CFD) packages (such as Ansys Fluent and CFX) has gradually become the main tool used to study GWVHT systems.

Vortex dynamics plays a central role in power generation in GWVHT systems [22]. However, the presence of a free-surface, air–water interaction, and turbine-induced disturbances makes the flow highly complex and difficult to characterize experimentally. The turbine alters the vortex structure by reducing tangential velocity and increasing axial and radial velocity components [23], while the formation of an air core further affects the stability and strength of the vortex [24,25]. Depending on operating conditions, the vortex can be classified as weak or strong [26], and its stability is influenced by secondary flows and sub-vortices [27]. This complexity limits the applicability of simple theoretical models and highlights the importance of CFD for understanding turbine–vortex interactions.

Several factors strongly affect the vortex dynamics, including inlet channels, shape and size of the basin, shape and number of the turbine blades, shape of the turbine, size and design of the discharge, and materials. The past studies further identified that the basin configuration and the turbine are the most crucial elements that dictate the performance of a GWVHT system in terms of power output and efficiency [8,28–33].

Numerous studies have investigated the effects of basin and inlet channel configurations on GWVHT performance [4,7,19–21]. Cylindrical basins with centrally located discharge orifices have been widely adopted, and an optimal ratio of discharge diameter to basin diameter in the range of 14–18% has been consistently reported [22]. Although conical and curved basin shapes can improve vortex strength, cylindrical basins have shown better scalability for practical systems. Velasquez et al. [8] recently reported a peak efficiency of 60.85% using a spiral inlet, cylindrical basin, and optimized runner placement, highlighting the strong influence of basin–inlet design on turbine performance.

As mentioned above, the turbine plays a key role in a GWVHT system. The type and number of runners (blades) in the turbine, and its position in the GWVHT system significantly affect the overall performance of the system, as they have a greater impact on the vorticity in the system [34–36]. A relation between the turbine geometry and the underlying flow during irrotational and rotation flow conditions is needed to capture the loss vorticity path in the behavior of vortex structure in the stationary and rotary regions in the basin [37]. To achieve this, an improved understanding of the turbine–vortex interaction is needed. Although successful in improving the efficiency of a GWVHT system, simple experimentally based designs were unable to provide the details of the internal flow characteristics caused by the turbine [38]. The overall efficiency was still under 50% [19].

Increasingly, numerical simulations have been widely used to explore the intrinsic features of a GWVHT system involving free-surface vortex and water–air interactions. For example, Edirisinghe et al. [29,30] carried out numerical simulation studies of the effects of different configurations of vortex turbine blades, including blade inclination, turbine height, vertical twist and horizontal curvature, blade number, and draft tube, by examining the air core behavior in terms of the detailed turbine–vortex interactions and velocity and pressure fields, whereas Nishi et al. [39] conducted numerical simulations to identify some key loss locations, such as the dominant in-tank and tank-outlet losses, followed by the in-tank friction losses. They also found that the blade losses generated inside the runner and the in-turbine friction losses were small, and additionally, there were also losses due to convergent paths and water–air interactions. Edirisinghe et al. [40] carried out a further numerical simulation study on a GWVHT system, focusing on the rotational speeds, flow rates, and water levels.

Other studies have also highlighted the importance of blade shape and air core behavior. Mulligan et al. [41] showed that the presence of the turbine increases flow complexity and that torque increases as the air core diameter decreases, suggesting that exces-

sively large turbines may disturb air core formation. Edirisinghe et al. [30] demonstrated that vertically twisted turbines do not always promote stable air core propagation, while Gupta et al. [42] reported efficiencies exceeding 50% using curved blades with blade-hub angles between 18° and 24°. More recently, Velásquez et al. [31] performed numerical optimization of a GWVHT runner in a conical basin with a spiral inlet channel and achieved efficiencies up to 65.18%.

Despite these advances, most existing studies focus on specific basin configurations, inlet designs, or isolated blade parameters. Systematic numerical comparison of fundamentally different blade geometries (such as flat, curved, and vertically twisted runners) under identical hydraulic and geometric conditions in a cylindrical basin remains limited. This lack of consistency makes it difficult to directly assess the relative merits of different blade shapes and to identify optimal operating conditions for practical GWVHT applications.

Recent work has increasingly combined controlled experiments with CFD to quantify how basin geometry, discharge/orifice ratio, and runner configuration alter vortex structure, air core behavior, and torque generation under ultra-low-head conditions. For example, experimental assessments with different inlet and discharge basin configurations have clarified the hydrodynamic effects of geometry on vortex behavior and performance metrics [8], and comparative CFD experimental studies have examined vortex profiles and turbulence model influences on the flow field [43]. Additionally, combined numerical and experimental analyses of small-scale gravitational vortex turbines have quantified performance characteristics under varying flow and geometric conditions [44]. Despite this progress, published datasets remain difficult to compare directly because operating conditions and geometries often vary simultaneously (e.g., basin shape, inlet arrangement, runner size, blade curvature/twist, and runner submergence), and studies also differ in numerical formulation (steady MRF versus fully transient approaches). Broader reviews of vortex turbine design note the continued need for consistent, like-for-like comparison across configurations and highlight remaining gaps in unified performance evaluation frameworks [45]. Consequently, a consistent, like-for-like numerical comparison of fundamentally different runner blade geometries under identical hydraulic and geometric conditions in a cylindrical basin remains limited—motivating the present parametric CFD study.

This study presents the evaluation of the effects of turbine blade shape, discharge orifice diameter, and rotation speed of a five-blade turbine rotating in a cylindrical basin of a low head gravitational water vortex hydro-turbine system. Three blade shapes (flat, curved, and vertical twist) with three discharge orifice diameters at the basin bottom (ratios of the orifice diameter to the basin diameter of 0.14, 0.16, and 0.20) are considered across five turbine rotation speeds (40, 60, 80, 100, 120 RPM (revolution/minute)). The effects are examined both qualitatively and quantitatively with numerical simulation results which employ Volume of Fluid, Moving Reference Frame, and SST $k-\omega$ turbulence model.

2. Methodology

2.1. Hydraulic Efficiency (η)

As depicted in Figure 1, the main components of a typical GWVHT system include an inlet water channel, an outlet water channel, a circular basin with an orifice on its bottom for the discharge of water in the basin to the outlet channel, a turbine with multiple blades, and a vertical shaft, where the blades are attached, which is also connected to the electricity generator. The inlet channel regulates the flow of water into the basin, so its design determines the velocity and distribution of the water flow, which affect the water vortex formation and turbine performance, while the basin dictates the vortex formation; thus, its shape, size, and design affect the vortex's stability and strength, which in turn determines the turbine performance [8]. The performance of a GWVHT system is essentially

not affected by the outlet channel but significantly affected by the other three components. The principle and the pertinent theories about the generation of electricity by extracting energy produced by the free-surface water vortex using the turbine are well described in some previous studies (e.g., [4,40]) and are therefore not detailed here.

The key output parameter to quantify the performance of a GWVHT system is the hydraulic efficiency of the vortex turbine (η), which represents the ratio between the extracted power from the system ($P_{extracted}$) and the available hydraulic power ($P_{available}$), as defined below [8,31,40].

$$\eta = \frac{P_{extracted}}{P_{available}}. \quad (1)$$

$P_{available}$ is calculated by the following equation:

$$P_{available} = \rho g H Q, \quad (2)$$

where ρ, g, H, and Q are the density of water (1000 kg/m^3), the gravitational acceleration (9.81 m/s^2), the hydraulic head (m), and the volume flow rate passing through the turbine (m^3/s), respectively. Q is estimated by the volume flow rate passing through the inlet channel. H is the summation of the relative pressure head, elevation head, and kinetic head across the GWVHT system. As reviewed by the present authors [7], different definitions and calculations for H have been used in previous studies. It is believed that the definition by Edirisinghe et al. [40] is appropriate and thus used in the present study. Edirisinghe et al. [40] argued that because a GWVHT system operates under the atmospheric pressure, the relative pressure head is zero, while the kinetic head is negligibly small as the flow rate is small. Hence it is fair and appropriate to quantify H by the difference between the inflow and outflow water levels.

$P_{extracted}$ is the power generated by the turbine shaft when water hits the turbine blades, and is calculated as follows [8,31,40]:

$$P_{extracted} = T\omega, \quad (3)$$

where T is the torque generated on the shaft and ω is the rotation speed of the turbine (rad/s), respectively. In the numerical simulations of the present study, several values of ω were pre-defined.

2.2. Configurations of the GWVHT System Considered

As the inlet water channel, the circular basin with the discharge orifice, and the turbine with multiple blades are the main components, their configurations and geometrical dimensions and the operating conditions are the key input parameters for a GWVHT system.

The most common shapes for basins are cylindrical and conical [7]. In the present study, cylindrical basins are used, as sketched in Figure 2. Different shapes of turbine blades were used and studied [7], with straight (flat), twisted, and curved turbine blades the most common [7,21,46]. In the present study, these three types of turbines are considered, with their configurations sketched in Figure 3.

Although experimental investigations of GWVHT systems are typically performed at laboratory scale for practical and economic reasons, real installations usually operate at larger field scales. Under appropriate similarity conditions, the fundamental vortex dynamics and turbine–flow interactions remain comparable, implying that a numerical model validated against laboratory measurements can be reliably extended to predict the performance of field-scale GWVHT systems.

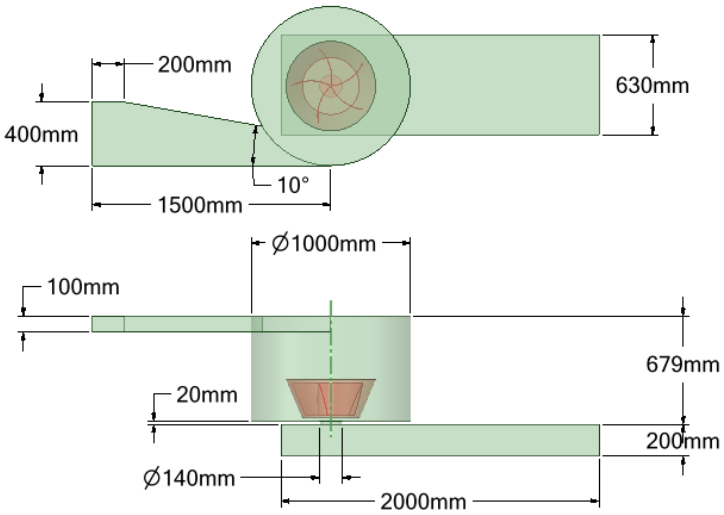

Figure 2. Schematic and geometrical dimensions of the GWVHT system considered: top view (top row) and side view (bottom row).

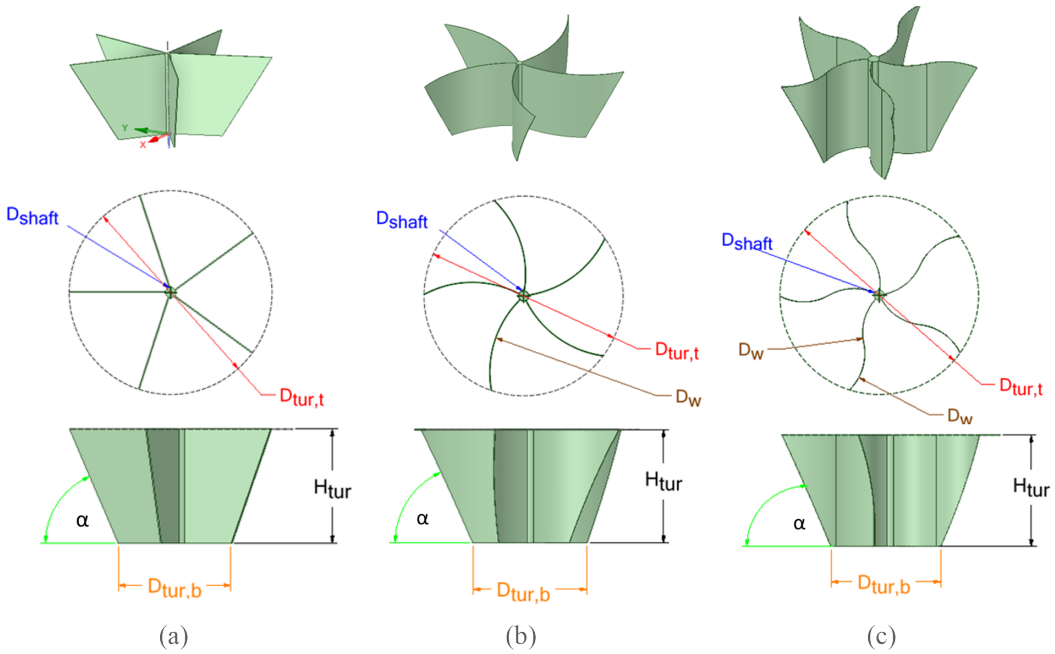

Figure 3. Geometrical configuration and dimensional parameters of the three runner types investigated: (**a**) flat-bladed runner, (**b**) curved-bladed runner, and (**c**) vertically twisted runner. For each configuration, the top, middle, and bottom rows show the isometric, top, and side views, respectively. The main geometric parameters used in the numerical model are indicated, including the shaft diameter D_{shaft}, the turbine top diameter $D_{\text{tur,t}}$, the turbine bottom diameter $D_{\text{tur,b}}$, the blade curvature diameter D_w (for the curved and vertically twisted runners), the turbine height H_{tur}, and the turbine inclination angle α.

To relieve the high demand to obtain numerical simulations, it is beneficial and appropriate to use a scaled down model of the prototype system (e.g., [40]). The scaled model of the GWVHT system for the numerical simulations in the present study can be created using the Froude number similarity [40], with the Froude number Fr defined as follows:

$$Fr = \frac{\text{Inertia force}}{\text{Gravity force}} = \frac{V}{(gL)^{1/2}}, \quad (4)$$

where V and L are the characteristic velocity (m/s) and length (m), respectively. In the present study, it is appropriate to choose the average velocity and length of the inlet channel as V and L, respectively.

The length scale factor used in the present study is $\lambda = 1/5$ (scaled model/prototype). With this length scale factor, the dimensions of the scaled model for the numerical simulations and the corresponding prototype system, along with the operation conditions, are listed in Table 1. The specific values of the dimensions and the operating conditions were determined based on the literature. It should be noted that as in the numerical simulations, the length of the inlet channel for the prototype system has no effect, so no scaling is applied to it. Similarly, as all geometrical dimensions of the outlet channel for both the prototype system and the scaled model have no influence on the system performance, no scalings are applied to them either. Three discharge diameters (0.14, 0.16, and 0.20 m) are considered in the present study to examine the effect of the discharge diameter.

Table 1. The dimensions of the main components of the GWVHT system and the operating conditions considered for the prototype and the scaled model for the numerical simulations ($\lambda = 1/5$).

Dimensions/Operating Conditions	Prototype	Scaled Model	Scale Factor
Operating conditions:			
Available power, $P_{available}$ (kW)	41.130	0.147	$\lambda^{3.5}$
Available head, h (m)	2.500	0.500	λ
Flow rate, Q (m^3/s)	1.654	0.030	$\lambda^{2.5}$
Free stream velocity, v (m/s)	1.923	0.86	$\lambda^{0.5}$
Inlet channel dimensions:			
Width, W_{inlet} (m)	2.0 (max)	0.4 (max)	λ
Length, L_{in} (m)	-	1.5	-
Height, H_{in} (m)	0.5	0.1	λ
Approach angle (degree)	10.0	10.0	-
Outlet channel dimensions:			
Width, W_{out} (m)	-	0.63	-
Length, L_{out} (m)	-	2.0	-
Height, H_{out} (m)	-	0.2	-
Basin dimensions:			
Diameter, d_b (m)	5.0	1.0	λ
Height, H_b (m)	3.295	0.659	λ
Discharge diameter, d_o (m)	0.7, 0.8, 1.0	0.14, 0.16, 0.2	λ

As shown in Figure 2, in the numerical simulations of the present study, the length of the inlet channel with the depth of 0.1 m is assumed to be 1.5 m away from the center of the basin, and its width varies. In the first 0.2 m section, the width is 0.4 m, and after that, the width reduces linearly toward the basin at the approach angle of 10°. The outlet channel of the depth of 0.2 m is assumed to be 2.0 m long and its horizontal shape is rectangular, with a width of 0.63 m. The diameter of the cylindrical basin is 1.0 m and its height is 0.659 m. The discharge orifice at the basin bottom protrudes downward to the water surface of the outlet channel by 0.02 m, and three values of the discharge orifice diameter (0.14 m, 0.16 m, and 0.20 m) were considered.

Each turbine is positioned at the bottom most position of the basin near the discharge orifice and is coaxial with the discharge orifice. The major parameters representing the turbine characteristics include the shape, number and size (dimensions) of the blades, the orientation and position of the blades in the basin, and the diameter of the shaft and/or hub on which the blades are attached. All these parameters affect the overall system performance. In the numerical simulations of the present study, as sketched in Figure 3,

all three types of turbines considered have 5 blades and the height (H_{tur}) and the bottom diameter ($D_{tur,b}$) of each turbine are fixed at 0.2 m while the top diameters ($D_{tur,t}$) are fixed at 0.4 m. The diameter of the shaft (D_{shaft}), where the blades are attached, is fixed at 0.02 m for each turbine. All turbines have a turbine inclination angle of $\alpha = 50^{\circ}$ to the vertical direction. For the curved turbine, each curved blade is of the curvature diameter of $D_w = 0.3$ m. For the vertical twisted turbine, each vertical twisted blade consists of two segments with the same length, with one curved clockwise and the other curved anti-clockwise at the same curvature diameter of $D_w = 0.3$ m. It was assumed that all turbines are submerged in water in the basin.

2.3. Numerical Simulation Method

As shown above, this study considered three types of turbine (flat, curved, and vertical twist) and for each turbine, three diameters of the discharge orifice were considered (0.14 m, 0.16 m, and 0.20 m), which form 9 configurations. For each configuration, five pre-defined values of ω (40 RPM, 60 RPM, 80 RPM, 100 RPM, and 120 RPM, where RPM is revolution per minutes) were used. These combinations create 45 numerical simulation cases. The Volume of Fluid (VOF) model, Moving Reference Frame (MRF) model, and SST $k-\omega$ turbulence model were used in the numerical simulation method of the present study. All these three-dimensional numerical simulations were carried out using ANSYS Fluent 2023 R2.

2.3.1. VOF, MRF, and SST $k-\omega$ Turbulence Model

The Volume of Fluid (VOF) model was employed to capture the air–water free-surface in the GWVHT basin. The VOF method solves a single set of momentum equations and tracks the volume fraction of each phase in every computational cell, allowing for accurate representation of the interface between immiscible fluids. This approach is particularly suitable for free-surface vortex flows, where strong interface deformation and air core formation occur.

The Moving Reference Frame (MRF) method was used to model the rotating turbine runner under steady-state conditions. In this approach, the governing equations are solved in a rotating coordinate system within a pre-defined sub-domain surrounding the runner, while the rest of the computational domain remains stationary. The MRF formulation provides an efficient approximation of rotor–stator interaction and is widely used for steady-state analysis of turbomachinery flows.

The SST $k-\omega$ turbulence model was adopted because it combines the advantages of the $k-\omega$ model in near-wall regions with the robustness of the $k-\varepsilon$ model in the free stream. This makes it particularly suitable for flows with strong adverse pressure gradients, flow separation, and swirling motion, which are characteristic of gravitational water vortex turbine systems.

For a GWVHT system, the generation of torque—thus, electricity—comes from the water vortices formed in the basin, which are generally free-surface turbulent flows. The performance of the system is dictated by the vortex dynamics, with the air–water–turbine interface playing a key role. For numerical simulations of such a two-phase (air and water) flow, the VOF model introduced by Hirt and Nichols [47] is the most appropriate and has been the most commonly used. In the previous studies on GWVHT systems, the VOF model has been extensively used (e.g., [15,23,28,31,37–40,48–55]). As the VOF model has been well documented in [47] and other sources and studies (e.g., ANSYS, Inc. provided detailed theory guides and tutorials to use it, and [39,56] described it in the context of hydropower turbines), the details of the VOF model are not presented here.

The flow in a GWVHT system is generally unsteady and turbulent, which results in a very high demand in computational power, cost, and time. To ease this, a MRF

model can be resorted. A MRF is defined as a reference frame moving with a prescribed orientation and speed with respect to a stationary reference frame. The incorporation of a MRF model in numerical simulations with moving objects has the benefit to convert a flow field, which is unsteady with respect to the stationary frame, to become steady with respect to the MRF [57]. In this way, only steady flow is needed to be numerically simulated, which substantially reduces the demand in computational power, time, and cost. The MRF model is relatively simple to implement and is very effective, efficient, and much cheaper to numerically simulate flows involving moving objects, particularly rotating objects, which makes it very popular and commonly used for rotational motion problems in turbomachinery applications including the hydropower turbines considered in the present study.

For the configuration of the GWVHT system considered in the present study, there are three stationary regions (the inlet channel and the outlet channel and the basin itself) and one rotational region (the fluid in the basin containing rotating turbine blades). When the MRF model is used for the systems containing rotating objects like the one considered in the present study, the velocity components in a defined region around the rotating turbine blades are transformed to a rotating reference frame [52,53,58]. In this way, instead of the blades moving physically through the water, the water moves around the blades with a corresponding velocity [59]. The governing equations for the motion are modified to take into account the additional acceleration terms that occur due to the transformation from the stationary to the Moving Reference Frame [60,61]. The flow around the moving parts is modeled by solving these equations in a steady-state framework. The fluid surrounding the rotor is considered to be rotating with the blades, and an absolute velocity formulation approach is chosen. With such a formulation, the governing equations are written with respect to the reference frame of the computational domain [52,58]. Torque (T) is the main output parameter for the present study and was monitored during the numerical simulations. With the obtained T, $P\_extracted = T\omega$ and thus the hydraulic efficiency η are calculated (with Equation (1)). As the introduction of the MRF model including the governing equations has been well documented (such as [57,59,62,63]), its details are not presented here too.

From the literature (e.g., [7]), it was noted that the most commonly used turbulent model for GWVHT systems and other very similar hydropower turbine systems is the SST $k-\omega$ turbulence model [31,37–40,49,52–54,56,58,60,64–71]. As the details of the SST $k-\omega$ turbulence model have been well documented (e.g., [52,63,67,68]), they are also not presented here as well.

2.3.2. Computational Domain and the Boundary Conditions

The computational domain and the boundary conditions for the numerical simulations of the present study are presented in Figure 4. The whole computational domain consists of three main regions: the inlet channel, the outlet channel, and the basin in which the rotating turbine sits. With the use of the MRF model, the whole computational domain is divided into two different domains in terms of the motion of fluid: the stationary domain, which includes the inlet and outlet channels and the basin itself, and the rotating domain, which is the space occupied by the fluid, noting the blades and the turbine shaft being stationary in the MRF model.

The boundary conditions at different boundaries are labeled in Figure 4. For all solid boundaries, no-slip boundary conditions were imposed. An inlet velocity of 0.86 m/s was imposed at the inlet channel, with this value calculated with the equation proposed by Velasquez et al. [28] through their study on the optimization of the inlet channel and basin. The upper surfaces of the channels (at the free surfaces) and basin were set at a static

pressure of 0 Pa, and air could enter and exit freely. The rotating domain was set to rotate with increments of 20 RPM from 40 RPM to 120 RPM.

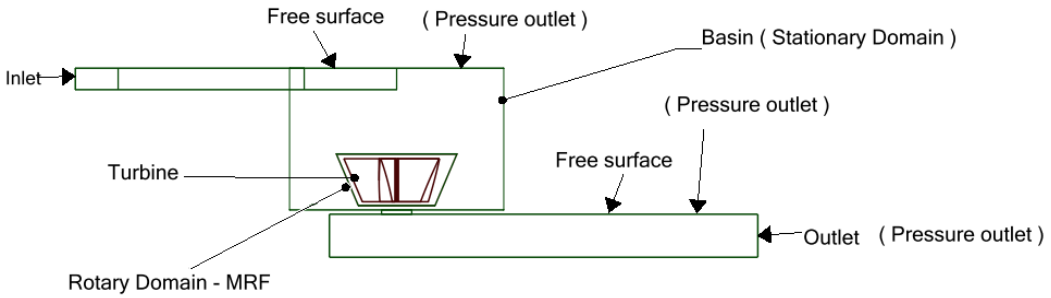

Figure 4. Computational domain and the boundary conditions.

2.3.3. Meshing of the Computational Domain

The 3D Modeling Software Spaceclaim in Ansys Fluent was used to model the geometry of the computational domain and create structured meshes using the in-built Mosaic Meshing Technology. Mosaic Meshing is an advanced meshing technology which conformally connects any type of mesh to any other type of mesh, making it possible to build optimal meshes that use the best type of element in every section of the mesh. It is particularly efficient for numerical simulations involving very complex computational domains like the one used in the present study. Polyhexcore meshes created with the Mosaic Meshing Technology were shown to shorten up to 50% of the simulation time when compared to hexcore or generalized polyhedral meshes of the same accuracy [72,73].

For the surface meshing, the clean geometry is imported and the global and local sizing parameters are assigned. In the present study, the minimum global cell size was 3 mm while the local fine cell sizing of 2 mm and 1 mm were applied to the two free-surface channels and turbine, respectively, to capture the VOF on the free-surface interface and the viscous forces at the turbine walls. The growth rate of the grid of 1.2 was applied. A skewness quality factor of 0.51 was achieved, indicating a good quality surface mesh. The surface meshing provides a good foundation for good volume meshing.

For volume meshing, the polyhexcore volume meshing type was used. Five inflation layers of cells were used on the outer layer to capture velocity and pressure gradients. The interior of the basin was meshed using structured polyhexcore cells and the orthogonal prism cell was meshed on the basin and blades. A total of 2.4 million cells were generated, resulting in a good orthogonal quality of 0.2.

The meshing created using the Mosaic Meshing Technology for the present study is presented in Figure 5.

A mesh independence test was conducted for the case in which the discharging diameter of the basin is 0.16 m and the turbine with 5 curved blades rotated at 80 RPM, with four different meshes. The details of the meshes and the mesh independence test results in terms of torque, which is the main output parameter to quantify the performance of the GWVHT system, are presented in Table 2. From the table, it is seen that the torque produced with the fine mesh with about 2.4 millions of elements and that with the finest mesh with about 3.6 millions of elements are essentially the same, indicating that the fine mesh can produce accurate simulation results; thus, it was chosen for all the numerical simulation of the present study. On the walls of this mesh, $y^+ < 5$ was ensured. This mesh has the volume elements which are slightly smaller than the 2.6 millions used by Edirisinghe et al. [40], but larger than those used by Velásquez et al. [15,28,31], Edirisinghe et al. [30], and Yosry et al. [56], which are some recent leading numerical studies on GWVHT systems.

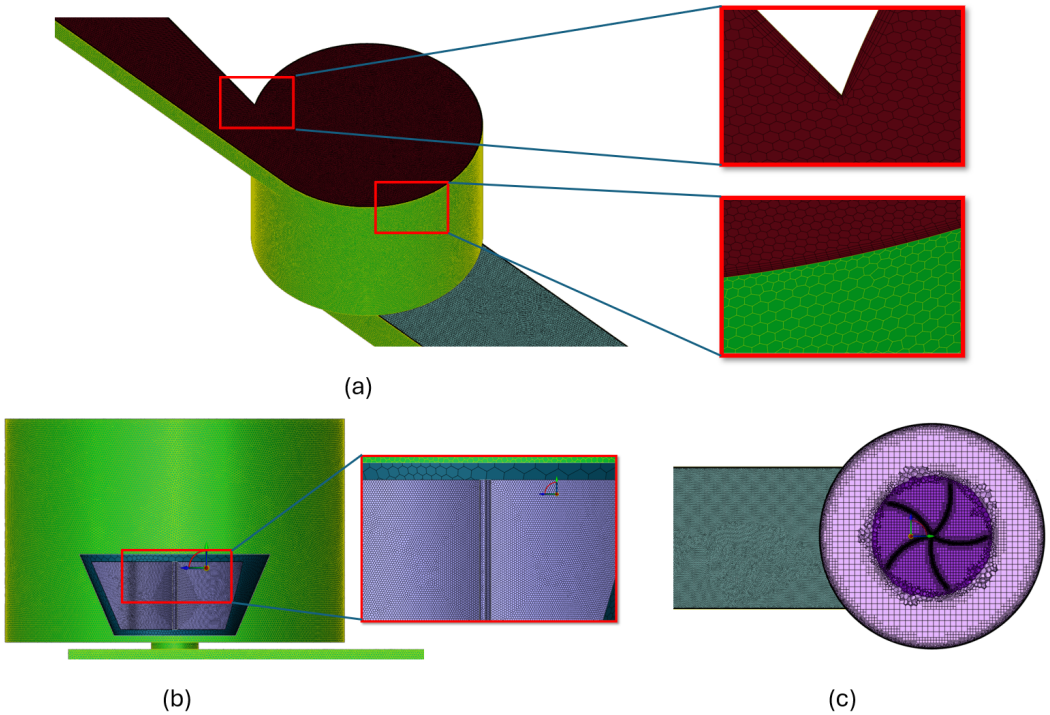

Figure 5. Meshing of the computational domains: (**a**) an isometric view of the surface meshing of the whole computational domain; (**b**) a 2D view of the volume meshing on a vertical plane through the rotation axis, focusing on the turbine; and (**c**) a 2D view of the volume meshing on a horizontal plane, focusing on the basin and the turbine, respectively.

Table 2. Mesh independence test results.

Mesh	Minimum Surface Element Size (m)	Rotary Domain	Stationary Domain	Total Volume Volume Elements	Torque (N·m)	Difference (%)
Coarse	0.029	925,880	135,624	951,721	3.949	17.2
Medium	0.019	913,375	218,221	1,131,596	4.767	0.3
Fine	0.003	2,013,127	390,295	2,403,422	4.781	0.08
Finest	0.0025	3,147,544	433,205	3,580,749	4.785	0

2.3.4. ANSYS Fluent Setup

All numerical simulations were carried out using ANSYS Fluent 2023 R2. In the Fluent setup, the flows were assumed to be three-dimensional and at the steady state. A homogeneous VOF multiphase model with water and air as fluid phases percentages (%) with the implicit volume fraction formulation was used. The open channel and the free-surface model were activated to allow for traction of the phase interfaces. The surface tension force modeling was switched on and the surface tension coefficient was set to be 0.072 N/m. The MRF model was selected to deal with the stationary and moving domains. The steady-state two-phase simulations were performed using the pressure-based coupled solver with pseudo-transient stabilization enabled. In this approach, the pseudo-time step is automatically and adaptively calculated by ANSYS Fluent based on the local mesh length scales and flow velocities through an internal Courant-number-based formulation. Therefore, no user-defined pseudo-time step was prescribed. Convergence was assessed not only by residual reduction (to at least 10^{-5}) but also by monitoring the stabilization of integral quantities, including turbine torque, output power, and global mass and volume fraction balance. A solution was considered converged only when all monitored variables reached steady and physically consistent values. The rotational speed was assigned starting from 40 RPM to 120 RPM with an increment of 20 RPM. The inlet boundary was assigned

at a constant velocity of 0.86 m/s. At the inlet, the water was assigned to a multiphase volume fraction of 1, indicating water is the primary fluid. The SST $k-\omega$ turbulence model was selected, with the turbulent intensity and turbulent viscosity ratio of 5% and 10 assigned respectively.

2.4. Validation

The numerical model was validated against the experimental configuration reported by Edirisinghe et al. [40], where the turbine geometry and operating conditions were reproduced based on the parameters available in the reference. The reason for this choice is that it is the most similar study which has both experimental and numerical results available for the validation purpose of the present study, and Edirinsinghe et al. validated their numerical simulation method with their experimental results. In the study by Edirinsinghe et al. [40], as sketched in Figure 6, a conical basin is used and the turbine used has 8 vertical twisted blades.

Figure 7 presents a direct validation of the present CFD model against the experimental measurements reported by Edirisinghe et al. [40], together with their corresponding numerical predictions. The comparison is performed for five turbine rotational speeds using the same configuration shown in Figure 6, and is based on both hydraulic efficiency (η, %) and torque (T, N·m).

In this figure, the dimensionless specific speed (N_s) used by Edirinsinghe et al. [40], as defined below, is used instead of the dimensional rotation speed (ω)

$$N_s = \frac{\omega P^{1/2}}{H^{5/4}}, \tag{5}$$

where ω is in RPM (rev/min) over 40 RPM–120 RPM, P is the power in kW, and H is the hydraulic head in m. In both the study of Edirinsinghe et al. [40] and the present study, $P = 0.04$ kW and $H = 0.45$ m were used, respectively.

From Figure 7, it can be seen that the numerical simulation results of the present study replicate the numerical simulations results of Edirinsinghe et al. [40] exceptionally well, with the maximum differences in η and T below 2% for all rotational speeds considered. This indicates that the numerical simulation method of the present study is validated. Small discrepancies between the numerical and experimental results may arise from uncertainties associated with free-surface instability, air–water interaction, turbulence model assumptions, interface capturing errors in the VOF method, grid resolution near the blade edges and free-surface, and experimental measurement limitations in highly unsteady vortex-dominated flows. Nevertheless, the observed agreement in both torque and hydraulic efficiency demonstrates that the present numerical framework reliably captures the dominant hydrodynamic behavior of the GWVHT system.

It should be noted that although the validation is performed using the configuration studied by Edirisinghe et al. [40], which differs from the cylindrical basin and blade geometries investigated in the present work, the excellent agreement with both experimental and numerical data confirms the general reliability of the numerical methodology prior to its application to the new turbine configurations considered in this study.

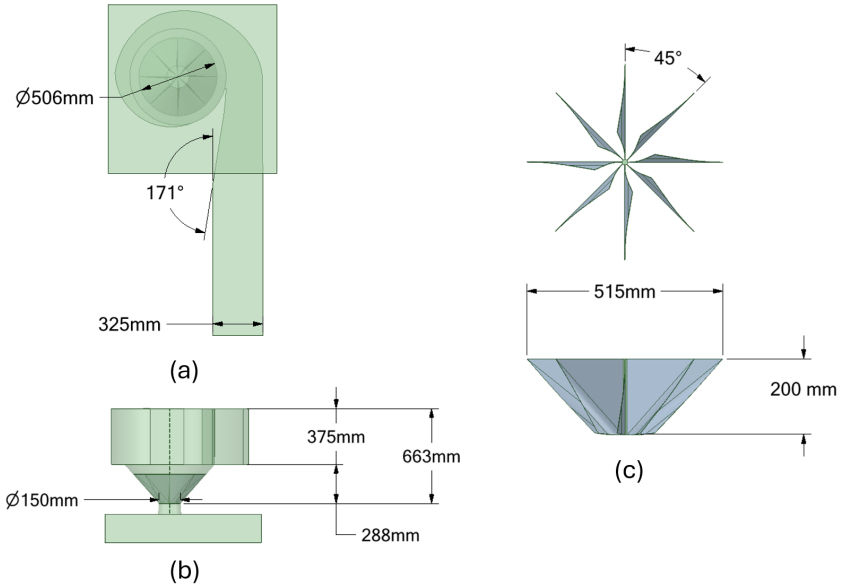

Figure 6. Schematic and the geometrical dimensions of the GWVHT system considered by Edirinsinghe et al. [40] for the validation: (**a**) top view, (**b**) size view, and (**c**) turbine blades (adopted from Edirinsinghe et al. [40]).

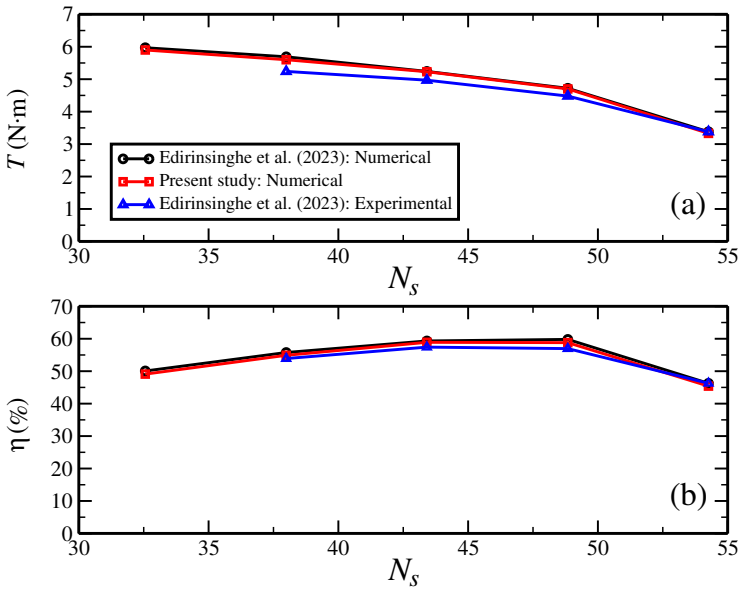

Figure 7. Comparison of the numerical and experimental results of Edirinsinghe et al. [40] and the numerical results of the present study for the validation: (**a**) hydraulic efficiency (η, %) and (**b**) torque (T, N·m).

3. Results and Discussion

3.1. Qualitative Analysis

For the qualitative analysis, the contours of water (Phase 2) fraction, pressure, velocity, and turbulent kinetic energy (k) on several vertical and horizontal planes are presented. These planes are depicted in Figure 8, which include five vertical $Y-Z$ planes at different X locations between 0.0 m and 0.4 m, five vertical $X-Y$ planes at different Z locations between 0.0 m and 0.4 m, and five horizontal $X-Z$ planes at different Y locations between 0.0 m and 0.4 m, respectively. However, when the comparisons are made to show the effects of blade shape, discharge diameter, and turbine rotation speed, only the contours on the two vertical planes (Plane 1, which is the vertical $Y-Z$ plane at $X = 0.0$ m, and Plane 2, which is the vertical $X-Y$ plane at $Z = 0.0$ m) are presented, although the contours on all

five horizontal $X - Z$ planes at five Y locations ($Y = 0.0$ m, 0.1 m, 0.2 m, 0.3 m, and 0.4 m, respectively) are still presented.

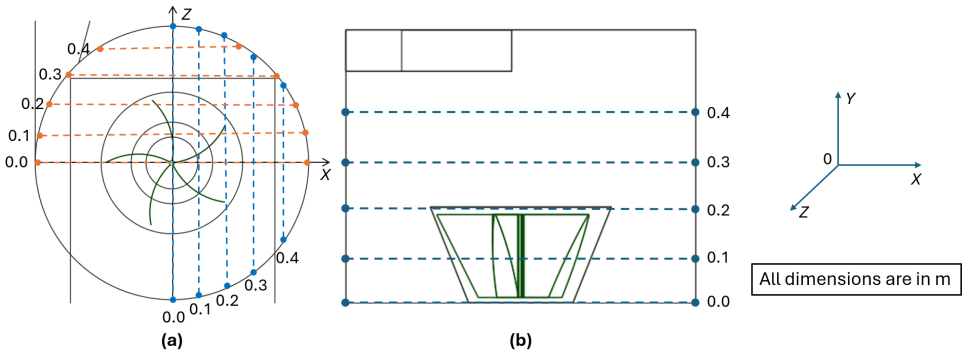

Figure 8. Sketch of the planes on which the contours of water (Phase 2) fraction, pressure, velocity, and turbulent kinetic energy (k) are presented for the qualitative analysis: (**a**) five vertical $Y - Z$ planes at different X locations between 0.0 m and 0.4 m and five vertical $X - Y$ planes at different Z locations between 0.0 m and 0.4 m; and (**b**) five horizontal $X - Z$ planes at different Y locations between 0.0 m and 0.4 m, respectively.

3.1.1. Representative Contours of Water Fraction, Pressure, Velocity, and k on Different Planes

To present an overview of the contours of water fraction, pressure, velocity, and k on different planes in the cylindrical basin, the specific case with five curved turbine blades which rotate at $\omega = 80$ RPM and with a discharge orifice diameter of $d_o = 0.16$ m is selected as an example. The results are shown in Figures 9–12 for the contours of water fraction, pressure, velocity, and k, respectively.

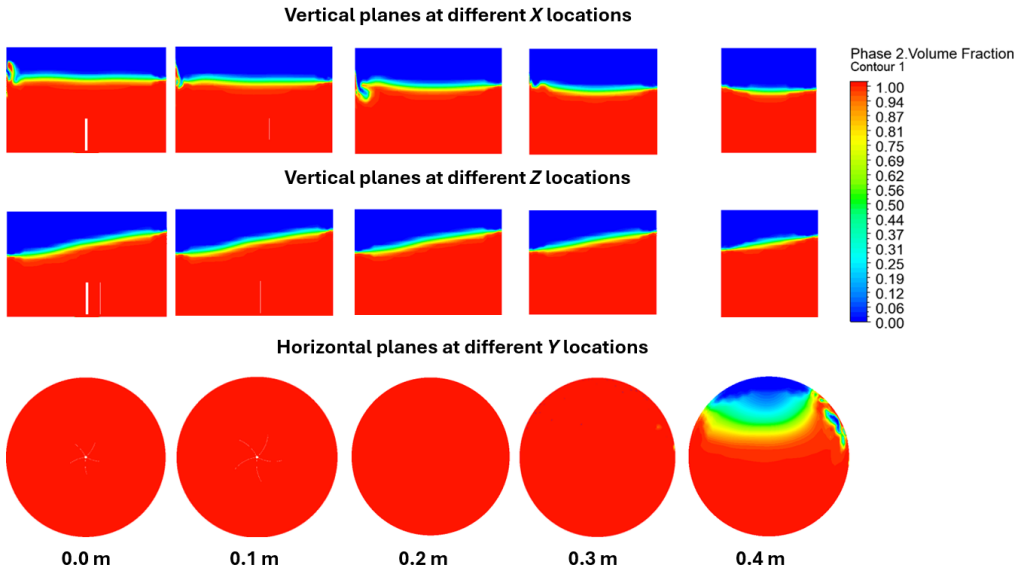

Figure 9. Contours of water (Phase 2) fraction on five vertical $Y - Z$ planes at different X locations (top row), five vertical $X - Y$ planes at different Z locations (middle row), and five horizontal $X - Z$ planes at different Y locations (bottom row) for the case with five curved turbine blades which rotate at $\omega = 80$ RPM and with a discharge orifice diameter of $d_o = 0.16$ m.

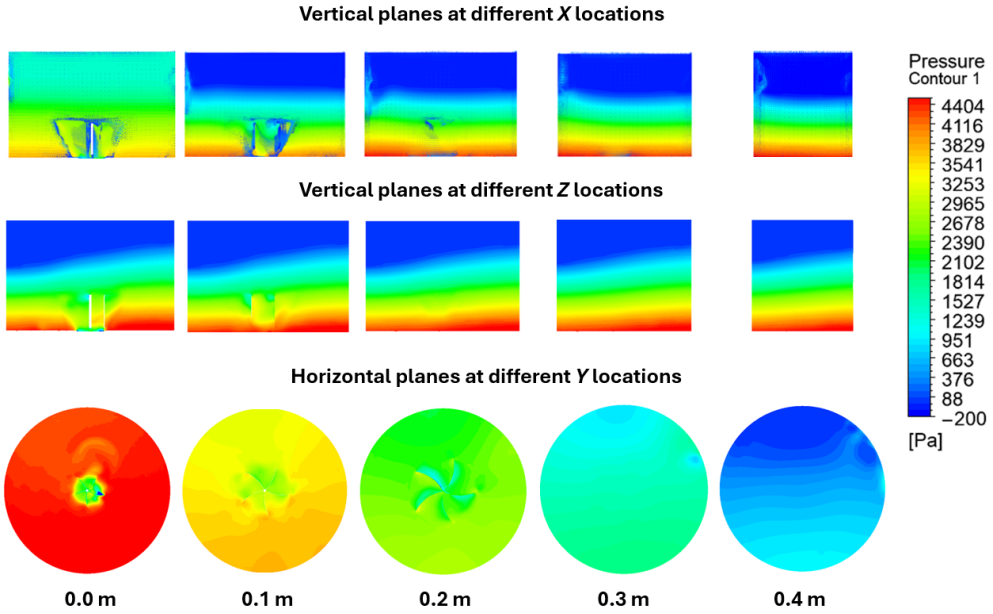

Figure 10. The corresponding contours of pressure on the same vertical and horizontal planes as those in Figure 9.

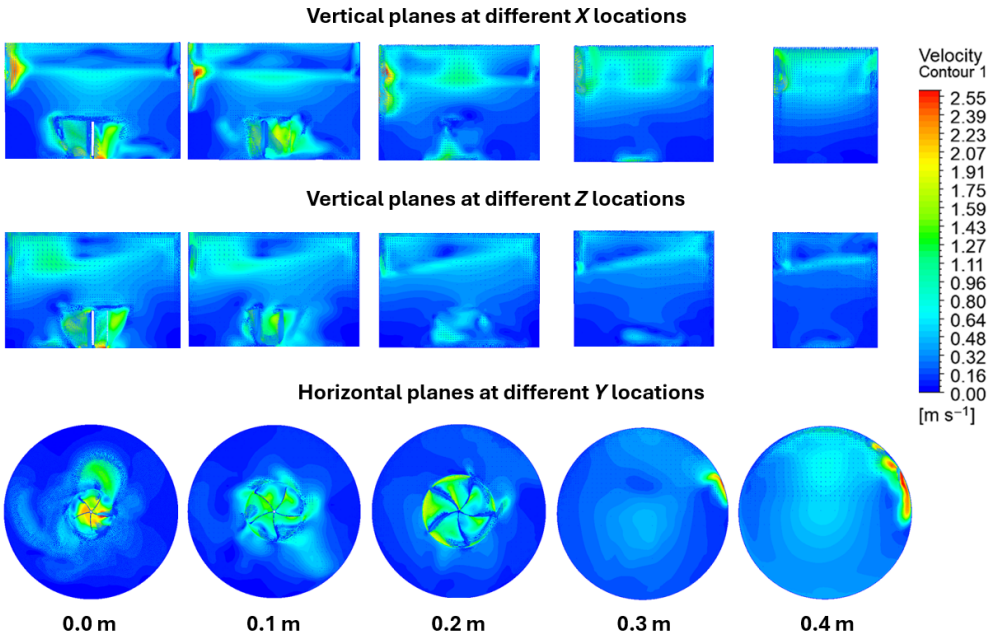

Figure 11. The corresponding contours of velocity on the same vertical and horizontal planes as those in Figure 9.

From Figure 9, it is seen that the lower region of the basin containing the turbine is fully occupied by water, while the upper region is dominated by air, indicating the formation of a stable free-surface vortex. This structure is governed by the strong radial pressure gradient generated by the swirling flow, where pressure decreases toward the vortex core and sustains the air–water interface and the development of the air core. The mixing layers observed at the interface correspond to regions of high shear between the rotating water and the air phase. Their nearly horizontal distribution on planes at different *X* locations suggests a largely axisymmetric vortex away from the inlet, whereas the locally thicker mixing regions near one side of the basin arise from inlet-induced asymmetry and blade-driven centrifugal effects. The inclined interface observed on planes at different *Z* locations

reflects the progressive strengthening of the vortex and pressure depression toward the discharge orifice, which is a characteristic feature of gravitational vortex systems [7,41].

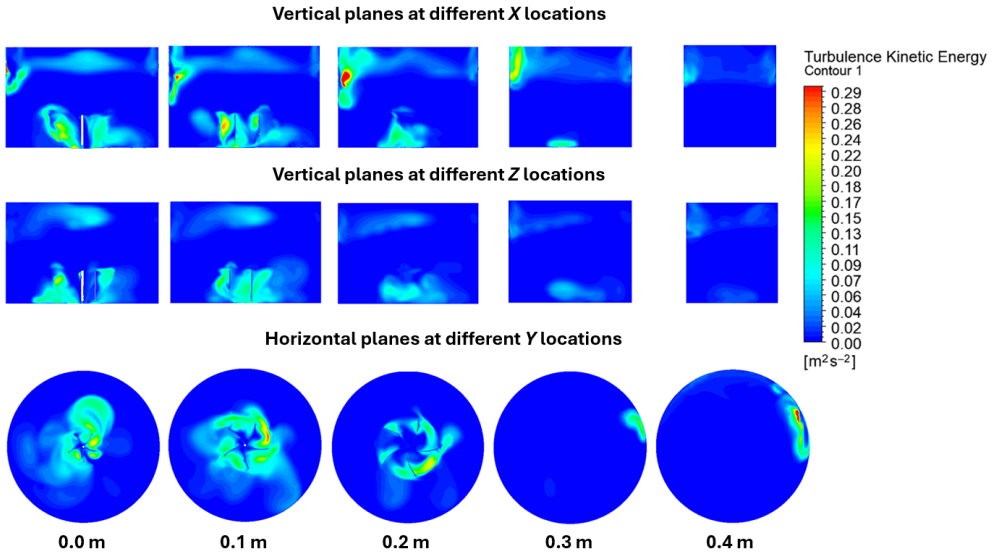

Figure 12. The corresponding contours of kinetic energy (k) on the same vertical and horizontal planes as those in Figure 9.

The pressure distributions at different vertical and horizontal planes vary significantly, particularly in the regions around the turbine and near the bottom, as shown in Figure 10. The pressure field plays a central role in vortex formation and energy conversion [74]. Three distinct regions can be identified along the vertical direction: a top region, a middle region whose lower boundary lies just above the turbine blades, and a bottom region containing the turbine. In the top region, the pressure remains close to atmospheric and nearly uniform, while the boundary between the top and middle regions coincides with the air–water mixing layer observed in the phase contours. Within this layer, pressure increases gradually downward, whereas in the core of the middle region, the pressure remains relatively uniform but significantly lower than in the bottom region. These low-pressure zones are responsible for the formation and stability of the free-surface (air core) vortex [7]. In a rotational vortex, the presence of high tangential velocities modifies the hydrostatic balance through a strong radial dynamic pressure field, which lowers the pressure toward the vortex center. The associated centrifugal acceleration, $\rho v_\phi^2 / r \sim \partial p / \partial r$, generated by the tangential velocity, v_θ, produces an inward pressure gradient that sharpens the mixing interface and sustains the low-pressure air core [7]. In the bottom region, the pressure increases markedly toward the discharge orifice as the flow accelerates downward through the small opening, indicating the concentration of kinetic energy near the turbine. In low-head vortex turbines, useful energy is extracted mainly from kinetic energy; accordingly, based on Bernoulli's principle, the velocity scales with $\sqrt{h}$, and the vortex redistributes this energy into tangential motion and pressure depression in the core, where energy extraction is most effective.

The velocity contours are presented in Figure 11. It should be noted that the horizontal tangential velocity (v_θ) at a particular point presented in the velocity contours is the relative velocity to the vertical plane, which rotates about the central axis at the same rotation speed (ω) as the turbine due to the use of the Moving Reference Frame (MRF) model, as described in Section 2.3.1, which is defined as a reference frame moving horizontally at ω with respect to a stationary reference frame (in this case, the stationary container wall and bottom). This means that the absolute horizontal tangential velocity with respect to the stationary container wall and bottom at the point should be the summation of the relative horizontal

tangential velocity presented in the contour and ωr, where r is the horizontal redial distance between the point and the central axis. The use of horizontal relative velocity contours is preferable as they can more explicitly illustrate the variations and distributions of velocity without the interference. Nevertheless, as the reference frame only rotates horizontally, the vertical velocity at a point is the absolute velocity with respect to the stationary container wall and bottom and is not affected by the rotation. From the figure, it is observed that the velocity distributions on each plane considered vary significantly and generally are not uniform. In the bottom region containing the turbine, velocities are large and vary notably within the turbine and its nearby area with strong shears at the tips of the blades, indicating intense blade–flow interaction and effective momentum exchange between the vortex and the runner, while far away from the turbine, the relative velocities are very small, indicating that the flow in such areas are essentially laminar and in a manner of rigid-body rotation of fluid, which is characteristic of a well-developed vortex flow. At the bottom ($Y = 0$ m), as expected from the conservation of mass, the relative velocities are the largest in a smaller area around the discharge orifice, as the water is discharged through the relatively very small exit orifice, reflecting strong flow acceleration toward the outlet. The distribution of the relative velocities in this small area is significantly not uniform due to the very strong turbulent behavior. Above the turbine ($Y = 0.3$ m and 0.4 m), the relative velocities are generally small, except at the entry location of the water in the inlet passage channel into the basin where they are very large due to the impingement of the water on the container wall, confirming that the inlet jet locally enhances the vortex strength and flow asymmetry.

Although the use of the MRF model affects the absolute horizontal tangential velocity at a point, the corresponding turbulent kinetic energy is not affected as k quantifies the variation in velocity, which is independent of the horizontal rotation of the MRF. The contours of k on different planes are shown in Figure 12. The results demonstrate that the characteristics of the distributions of k are very similar to that of the velocity, as shown in Figure 11. It clearly shows that the turbulence occurs mainly in the areas around the turbine with the strongest turbulence occurring at the tips of the blades, around the discharge orifice, and at the entry location of the water in the inlet passage channel into the basin, which correspond to regions of strong velocity gradients, flow separation, and intense vortex–blade interaction. For the majority of the remaining regions in the basin, the values of k are negligible, confirming that the flow is essentially laminar and in a manner of rigid-body rotation of fluid, indicating that the large-scale vortex motion is stable and only weakly dissipative away from the turbine and inlet zones, as revealed above from the velocity contours.

3.1.2. Effects of Turbine Blade Shape

To examine qualitatively the effect of turbine blade shape, the contours of water fraction, pressure, velocity, and k on Plane 1, Plane 2, and five horizontal $X - Z$ planes at $Y = 0.0$ m, 0.1 m, 0.2 m, 0.3 m, and 0.4 m, respectively, are presented for the three blade shapes (curved, flat, and vertical twist) for the three cases in which the turbines rotate at $\omega = 80$ RPM and the discharge orifice diameter is $d_o = 0.16$ m. These contours are shown in Figures 13–16, respectively.

Figure 13 demonstrates that, for all three turbine blade configurations, the lower two-thirds of the basin is entirely occupied by water, whereas the upper one-third is predominantly filled with air. Distinct mixing layers are evident at the air–water interface on the two vertical planes and the horizontal plane at Y = 0.4 m considered. Notably, the thickness and geometric profiles of these layers vary considerably depending on the blade shape. For the cases with curved and vertically twisted blades, the mixing layers exhibit comparable thicknesses and profiles. On Plane 1, the layers are largely horizontal,

although pronounced localized mixing occurs near one side of the basin, which is attributed to the centrifugal forces generated by turbine rotation in conjunction with the specific inflow location of water through the inlet passage. The extent of this localized mixing is markedly greater for the vertical twisted blades than for the curved blades, underscoring subtle differences in their hydrodynamic influence. On Plane 2, the mixing layer profiles for both curved blade types are inclined in the same direction, with similar thicknesses, a similarity likely arising from their shared curved geometries. In contrast, the flat blades produce mixing layers that diverge substantially from those associated with curved blades. On both planes, the layers are thicker and exhibit distinct profiles. On Plane 1, the mixing layer is slightly inclined, and no strong localized mixing region is observed near the basin wall, unlike the cases with the curved blades. On Plane 2, the mixing layer is nearly horizontal, yet a pronounced localized mixing region emerges near one side of the basin—an effect absent in the curved blade configurations. These pronounced differences in mixing layer behavior across the three blade types, as observed on Plane 1 and Plane 2, are further corroborated by the contours on the horizontal plane at Y = 0.4 m, indicating that blade geometry directly controls the strength and stability of the vortex-induced free-surface depression through its influence on local swirl intensity and air–water interaction.

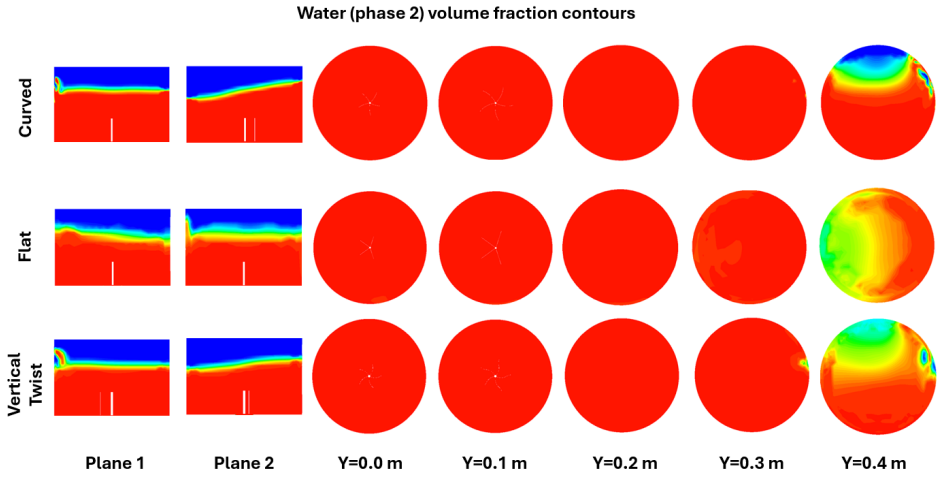

Figure 13. Comparison of the contours of water (Phase 2) fraction on two vertical planes (Plane 1 and Plane 2) and five horizontal $X-Z$ planes at different Y locations for the three turbine blade types (curved: top row; flat: middle row; vertical twist: bottom row), all at $\omega = 80$ RPM with $d_o = 0.16$ m. The scales for the water volume fraction contours are the same as shown in Figure 9.

From Figure 14, it is seen that the pressure contours associated with the three turbine blade configurations exhibit notable differences across all planes considered, despite sharing certain common features previously described for the curved blade case. The contours for the two curved blade configurations are broadly similar, reflecting their comparable geometrical characteristics, whereas the flat blade configuration demonstrates distinct deviations. A notable distinction arises in the boundary profile between the upper and middle regions on Plane 2. For the curved blade turbines, this boundary inclines in a direction opposite to that with the flat blades. Additional differences are evident in the thickness of the near-bottom regions, away from the turbine, where pressure increases downward with steep gradients. Furthermore, the pressure distributions across the horizontal planes reveal clear variations among the three blade types. Once again, the curved blade configurations exhibit comparable patterns, while the flat blades produce noticeably different distributions, showing that changes in blade geometry modify the local pressure recovery and redistribution of momentum, which in turn alters the structure and strength of the pressure field driving the vortex flow.

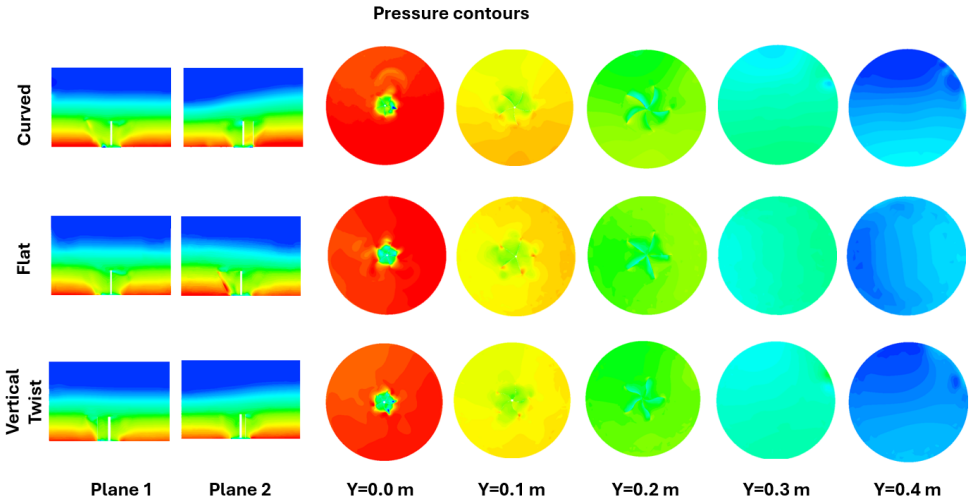

Figure 14. Comparison of the corresponding contours of pressure on the same vertical and horizontal planes as those in Figure 13. The scales for the pressure contours are the same as shown in Figure 10.

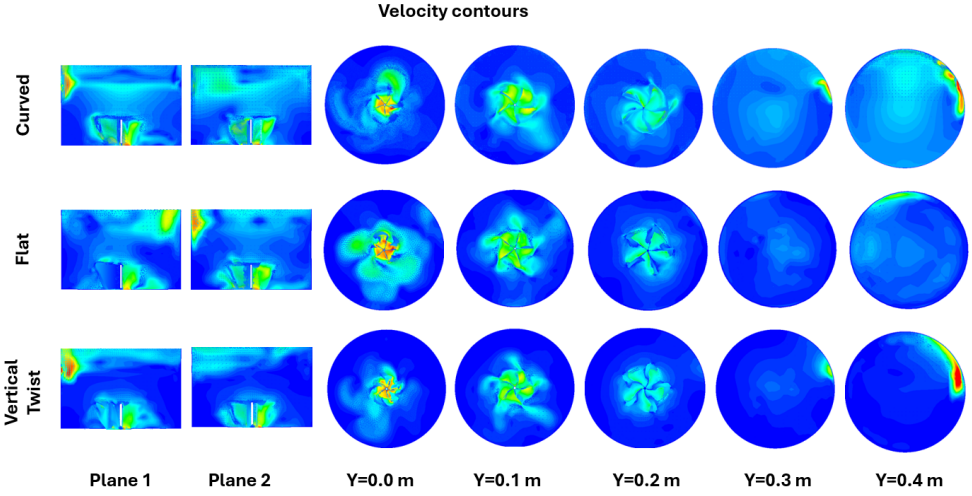

Figure 15. Comparison of the corresponding contours of velocity on the same vertical and horizontal planes as those in Figure 13. The scales for the velocity contours are the same as shown in Figure 11.

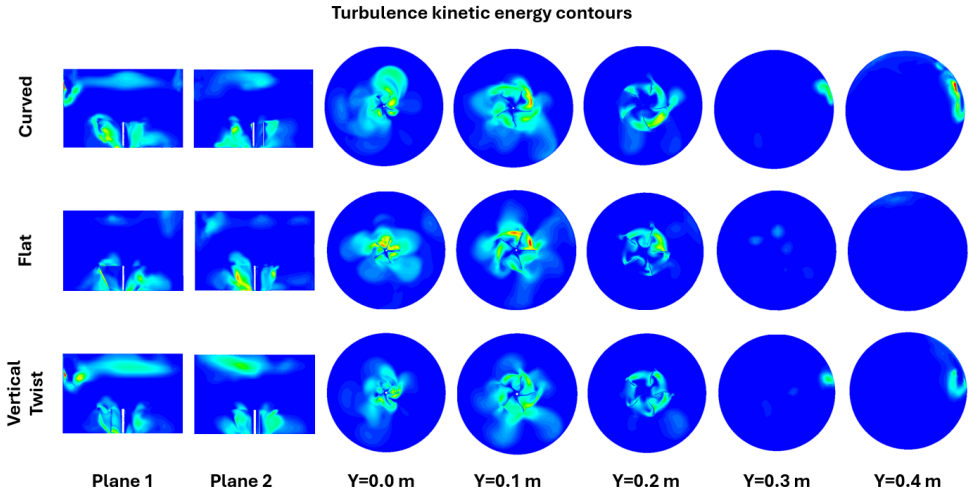

Figure 16. Comparison of the corresponding contours of k on the same vertical and horizontal planes as those in Figure 13. The scales for the contours of k are the same as shown in Figure 12.

Similarly, Figures 15 and 16 reveal that, across all three turbine blade configurations, the velocity and k contours on each plane exhibit discernible differences, while retaining

certain common features previously noted for the curved blade case. The contours corresponding to the two curved blade designs are broadly comparable, reflecting the influence of their similar geometrical curvature. In contrast, the flat blade configuration produces contours that deviate from these patterns, underscoring the distinct hydrodynamic behavior associated with its geometry.

3.1.3. Effects of Discharge Orifice Diameter

To examine qualitatively the effect of discharge orifice diameter (d_o), the contours of water fraction, pressure, velocity, and k on Plane 1, Plane 2, and five horizontal $X-Z$ planes at $Y = 0.0$ m, 0.1 m, 0.2 m, 0.3 m, and 0.4 m, respectively, are presented for the three discharge diameters considered ($d_o = 0.14$ m, 0.16 m, and 0.20 m) for the three cases in which the turbines rotate at $\omega = 80$ RPM. These contours are shown in Figures 17–20, respectively.

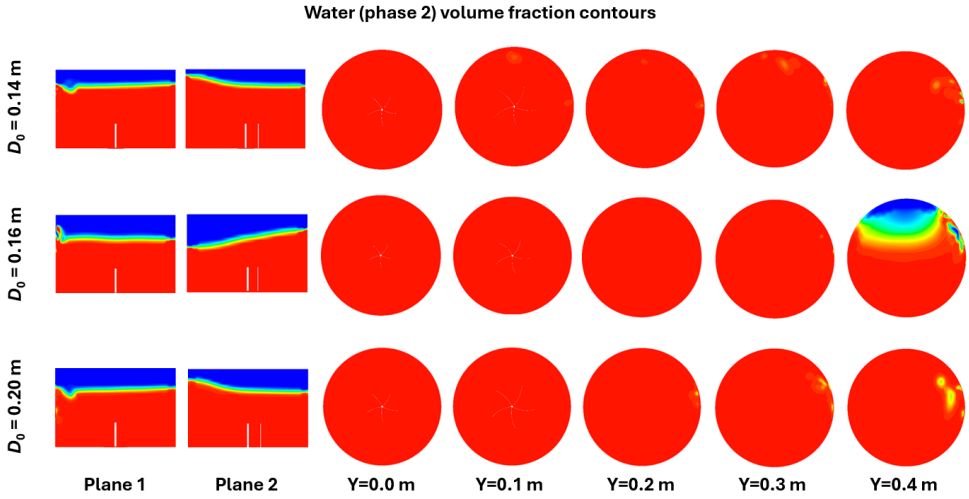

Figure 17. Comparison of the contours of water (Phase 2) fraction on two vertical planes (Plane 1 and Plane 2) and five horizontal $X-Z$ planes at different Y locations for the three discharge diameters ($d_o = 0.14$ m: top row; $d_o = 0.16$ m: middle row; $d_o = 0.20$ m: bottom row), all with curved blades rotating at $\omega = 80$ RPM. The scales for the water volume fraction contours are the same as shown in Figure 9.

From Figure 17, it can be seen that the discharge orifice diameter has a significant effect on the water distributions and vortex structure, particularly along the vertical direction, as illustrated by the contours on Plane 1 and Plane 2. It is interesting to note that the profiles of the mixing layer for the $d_o = 0.14$ m and $d_o = 0.20$ m cases are geometrically similar, although thicknesses and the volumes of the water-occupied regions differ. The profile and thickness of the mixing layer for the $d_o = 0.16$ m case are noticeably different, not only on Plane 1 and Plane 2, but also on the horizontal plane at Y = 0.4 m. The size of the water-occupied region for the $d_o = 0.20$ m case is also larger than those for the $d_o = 0.14$ m and $d_o = 0.20$ m cases. Such differences demonstrate that the influence of the discharge orifice diameter on the vortex-induced free-surface structure and water distribution is non-monotonic and governed by a complex interaction between flow contraction, vortex strength, and air core development.

From Figure 18, it is seen that the pressure contours for the three discharge orifice diameters exhibit clear differences in both magnitude and spatial distribution across all planes considered, although sharing certain common features previously described for the curve blade case at $d_o = 0.16$ m. For all three d_o cases, the sizes and profiles of the boundaries between two adjacent pressure regions differ significantly, consistent with the corresponding variations observed in the water-air interface structure. For the $d_o = 0.14$ m case, the relatively small discharge opening restricts the outflow, resulting in a larger and

thicker region of elevated pressure gradients and strong turbulence on the basin bottom away from the orifice. When d_o increases, water can be discharged more easily through the orifice, leading to a reduction in both the extent and thickness of the highly turbulent bottom region. The smaller and thinner turbulent area on the bottom, away from the turbine, for the $d_o = 0.16$ m case, compared to those for the $d_o = 0.14$ m and $d_o = 0.20$ m cases, indicates that the effect of the discharge diameter on the pressure field and associated vortex dynamics is non-monotonic, reflecting a balance between flow contraction at the orifice, vortex strength, and pressure recovery in the basin.

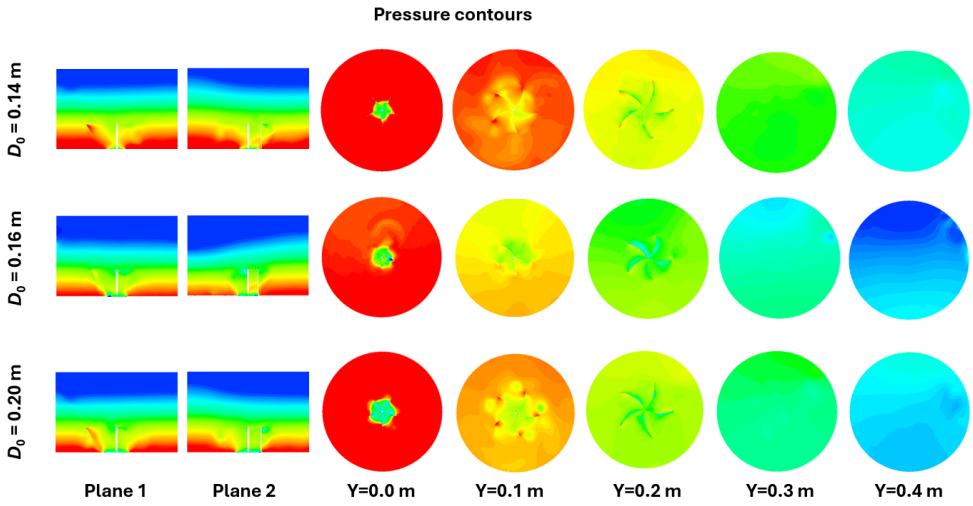

Figure 18. Comparison of the corresponding contours of pressure on the same vertical and horizontal planes as those in Figure 17. The scales for the pressure contours are the same as that shown in Figure 10.

The effect of the discharge orifice diameter is more evidently illustrated by the velocity and k contours, as shown in Figures 19 and 20. However, for the three d_o cases, the velocity and k contours on each plane exhibit significant differences, while retaining certain common features previously noted for the $d_o = 0.16$ m case. Again these contours further confirm the non-monotonic nature of the flow with d_o.

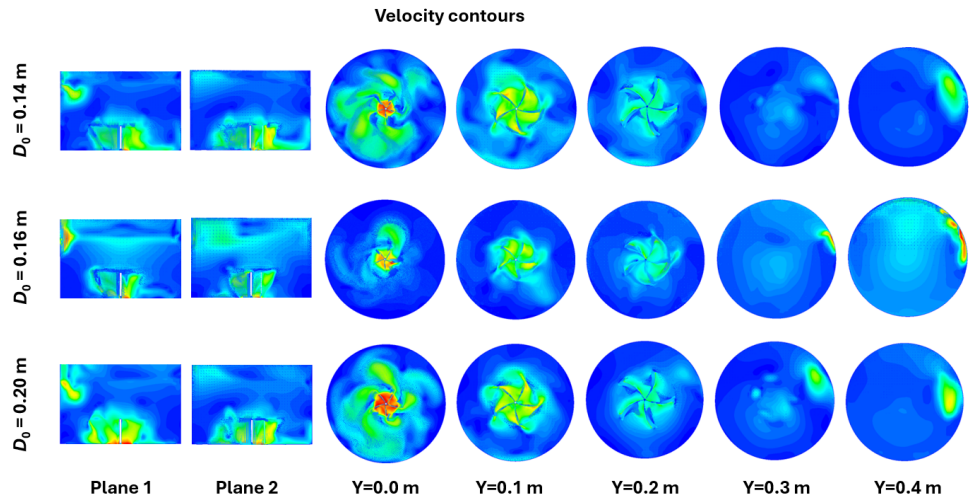

Figure 19. Comparison of the corresponding contours of velocity on the same vertical and horizontal planes as those in Figure 17. The scales for the velocity contours are the same as that shown in Figure 11.

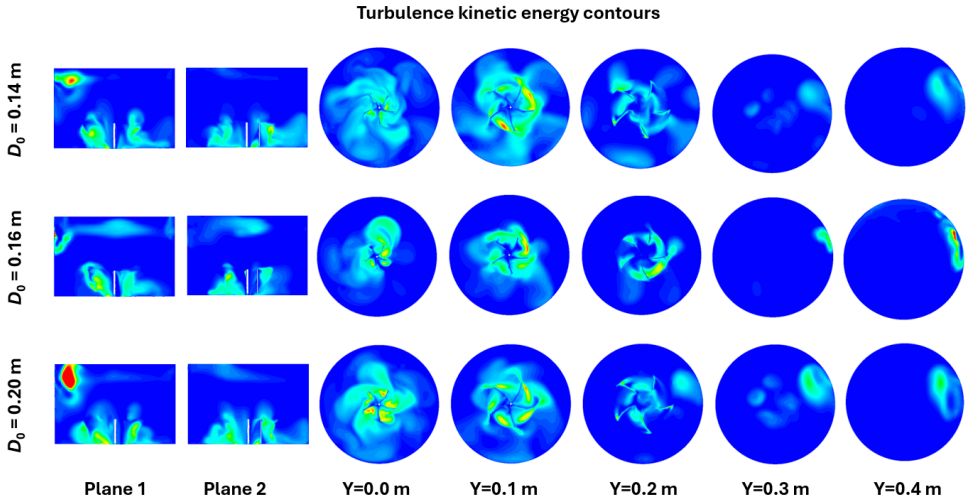

Figure 20. Comparison of the corresponding contours of k on the same vertical and horizontal planes as those in Figure 17. The scales for the k contours are the same as shown in Figure 12.

3.1.4. Effects of Turbine Rotation Speed

To examine qualitatively the effect of turbine rotation speed (ω), the contours of water fraction, pressure, velocity, and k on Plane 1, Plane 2, and five horizontal $X - Z$ planes at $Y = 0.0$ m, 0.1 m, 0.2 m, 0.3 m, and 0.4 m, respectively, are presented for the five turbine rotation speeds considered ($\omega = 40$ RPM, 60 RPM, 80 RPM, 100 RPM, and 120 RPM) for the five cases in which the turbine blades are curved and the discharge orifice diameter is 0.16 m. These contours are shown in Figures 21–24, respectively.

From Figure 21, it can be seen that the rotational speed of the turbine (ω) has a significant effect on the water distribution and the dynamic vortex characteristics, particularly along the vertical direction, as illustrated by the contours on Plane 1 and Plane 2, as well as on the horizontal plane at Y = 0.4 m. Although all cases with five different rotational speeds share some common water distribution patterns as that for the case with $\omega = 80$ RPM, the variations in the mixing layer thickness and the size of the water-occupied region indicate changes in vortex strength and air–water interaction with increasing ω. The results clearly show that, similar to the effect of d_o, the variation in the water distribution is not monotonic with rotational speed, as the sizes and the profiles of the mixing layer of the water region change in a non-linear way.

From Figure 22, it is seen that the pressure contours for all rotational speeds exhibit significant differences across all planes considered, although sharing certain common features previously described for the curve blade case at $d_o = 0.16$ m and at $\omega = 80$ RPM. For all rotational speeds, the sizes and profiles of the boundaries between two adjacent pressure regions differ significantly, consistent with the corresponding variations observed in the water-air interface structure. At low rotational speeds (40 RPM and 60 RPM), the profiles of the boundary between the top region and the middle region are basically horizontal on Plane 1 and Plane 2. But with the increase of rotational speed, although the profiles of the boundary between the top and middle regions are essentially horizontal on Plane 1, they incline on Plane 2 , reflecting the strengthening and asymmetry of the swirling flow and the associated radial pressure gradient. The inclination direction varies significantly and in a non-monotonic manner , highlighting the complex balance between vortex intensification and flow stability at different rotational speeds. The thickness of the region on the bottom, away from the turbine, also varies significantly and non-monotonically. The pressure distributions on the horizontal planes at different heights are notably different, reflecting the sensitivity of the vortex-driven pressure field to changes in turbine rotational speed.

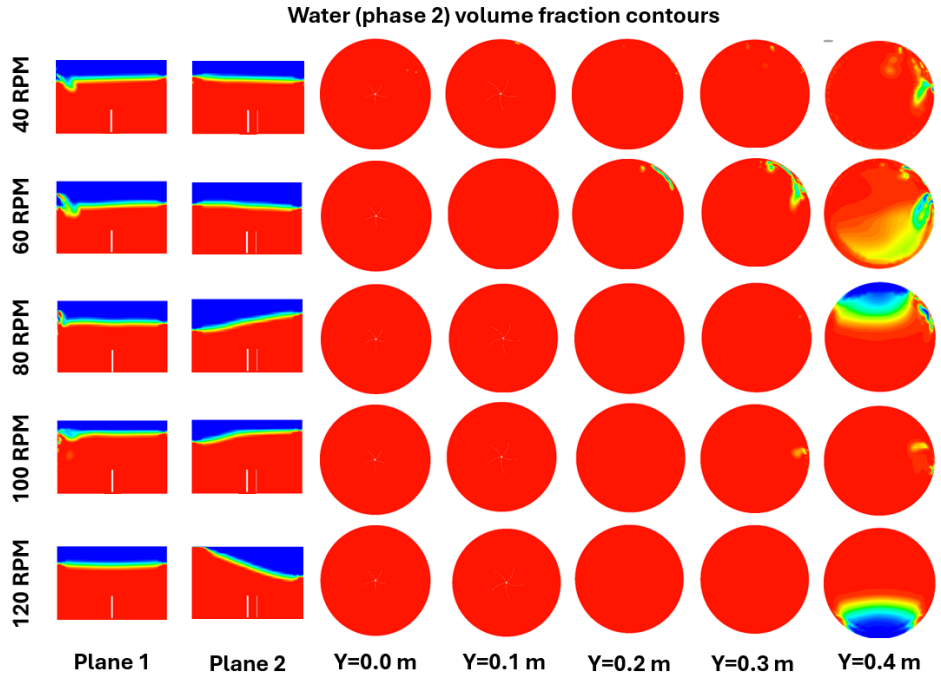

Figure 21. Comparison of the contours of water (Phase 2) fraction on two vertical planes (Plane 1 and Plane 2) and five horizontal $X - Z$ planes at different Y locations for the five turbine rotation speeds ($\omega = 40$ RPM: top row; $\omega = 60$ RPM: second row; $\omega = 80$ RPM: third row; $\omega = 100$ RPM: fourth row; $\omega = 120$ RPM: bottom row), all with curved blades and $d_o = 0.16$ m. The scales for the water volume fraction contours are the same as shown in Figure 9.

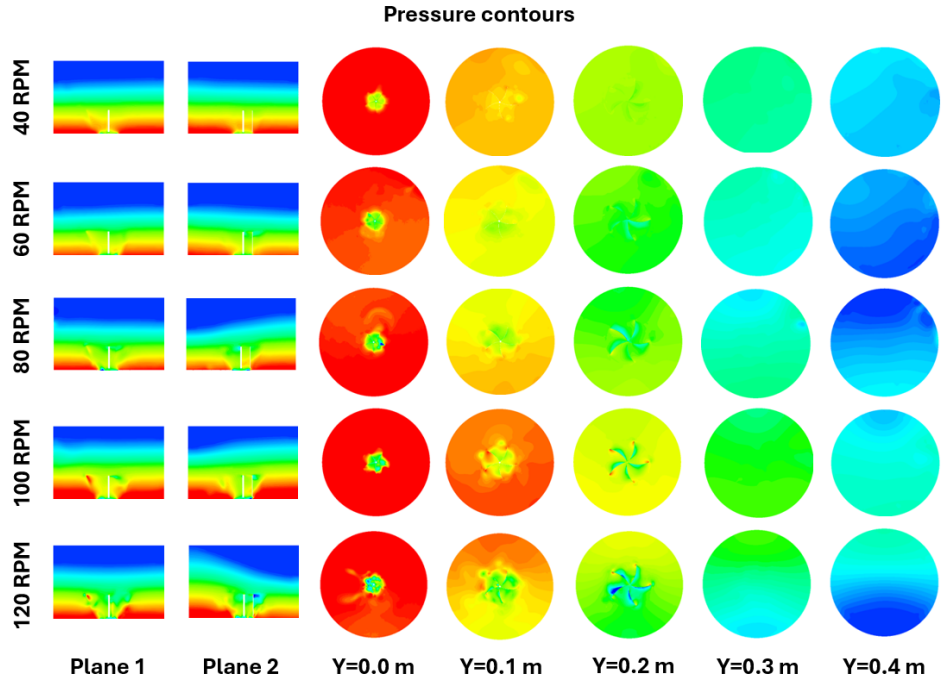

Figure 22. Comparison of the corresponding contours of pressure on the same vertical and horizontal planes as those in Figure 21. The scales for the pressure contours are the same as that shown in Figure 10.

The significant effect of rotational speed is also illustrated by the velocity and turbulent kinetic energy contours, as shown in Figures 23 and 24. In general, it is observed that with the increase of rotational speed, the velocity and turbulent kinetic energy increase on all planes with significant differences, but they still retain certain common features previously noted for the $\omega = 80$ RPM case as described above. The decreased turbulence in the top

region and increased turbulence in the bottom region, particularly around the blade tips when rotational speed increases, also confirm the non-monotonic effect of rotational speed observed from the distributions of water and pressure as described above.

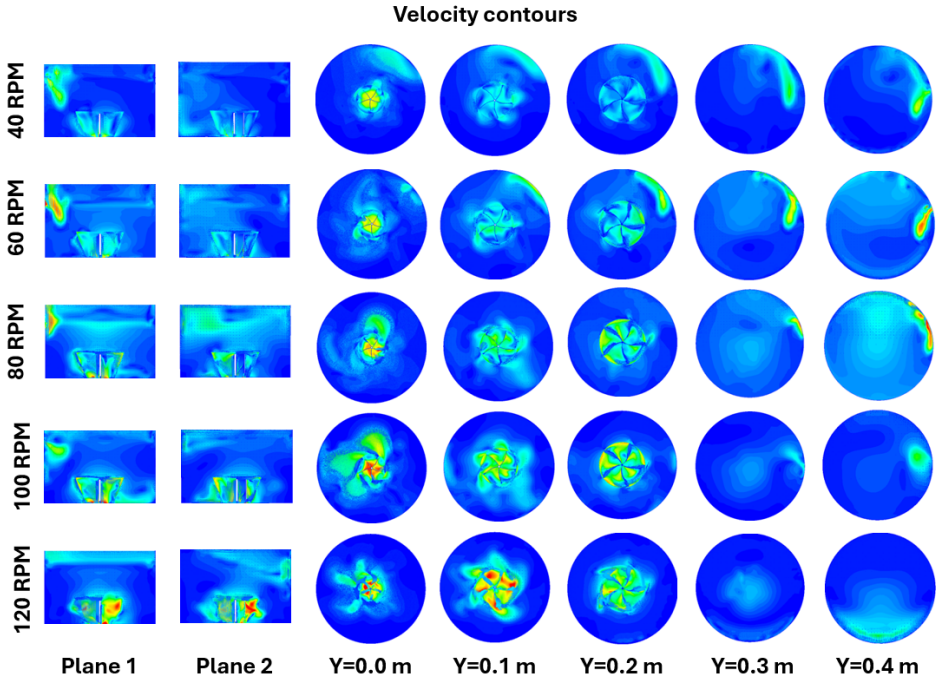

Figure 23. Comparison of the corresponding contours of velocity on the same vertical and horizontal planes as those in Figure 21. The scales for the velocity contours are the same as that shown in Figure 11.

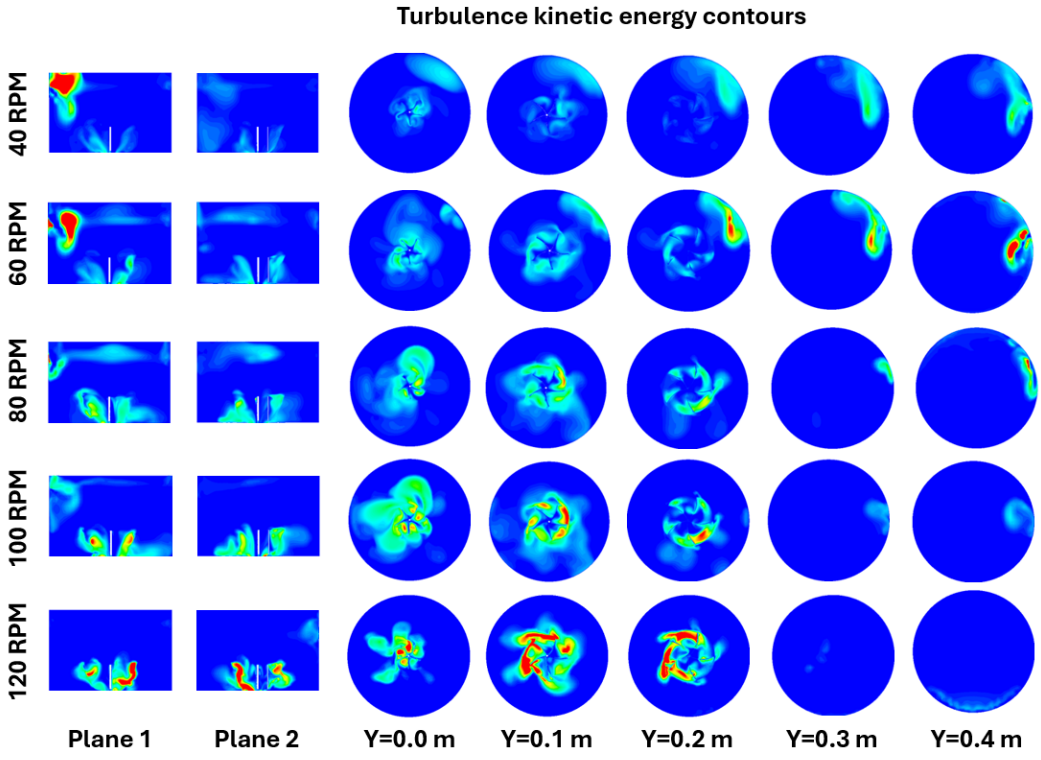

Figure 24. Comparison of the corresponding contours of k on the same vertical and horizontal planes as those in Figure 21. The scales for the k contours are the same as shown in Figure 12.

3.2. Quantitative Analysis

3.2.1. Torque, Power, and Efficiency

The numerically obtained values of torque, power, and efficiency for all cases considered are plotted against rotational speed in Figures 25 and 26. Although the data presented in these two figures are the same, the repetition is beneficial as the individual effect of the discharge orifice diameter and blade shape can be more explicitly and separately observed from Figure 25 and Figure 26, respectively.

From Figure 25, it is seen that for each type of turbine blade and each discharge orifice diameter, the generated torque (T) increases almost linearly at a large rate (around 0.2 N·m/RPM) when the rotational speed increases from 40 RPM to 80 RPM and then decreases, also essentially linearly, at a much smaller rate (around -0.08 N·m/RPM) when the rotational speed is further increased from 80 RPM to 120 RPM, clearly illustrating the significant but non-monotonic effect of rotational speed on the turbine system performance, which is in agreement with the qualitative results as described above. As the generated power ($P_{extracted}$) is $T\omega$, as defined by Equation (3), and the efficiency (η) is calculated by the ratio of $P_{extracted}$ and the available power ($P_{available}$, which is defined by Equation (2) and is 147 W in the present study as shown in Table 1), as defined by Equation (1), it is seen that the corresponding power and efficiency follow a similar trend when rotational speed increases, although both decrease at a significantly smaller rate when the rotational speed increases from 80 RPM to 120 RPM compared to torque. Such trends are in line with the findings in [38,75], i.e., torque stalls after certain RPM whilst turbulence increases, thus highlighting the inefficiency of high speeds, and beyond stalled torque, the energy derived from increased turbulence is dissipated into the small eddies instead of useful rotation. The results indicate that at a rotation speed of 80 RPM, all turbine systems attain maximum efficiency (between 40% and 62%, which are very good outcomes for such low head gravitational water vortex hydro-turbine systems). However, when the rotation speed is reduced, the efficiency drops dramatically, suggesting that the system should not operate at low rotation speeds. On the other hand, making the system run at higher than 80 RPM will not further improve the system performance, but on the contrary, will reduce the system performance, although the deterioration is not significant. It is observed that the highest efficiency and torque are consistently obtained at 80 RPM for all cases considered. This behavior can be attributed to an optimal balance between vortex stability and turbine–vortex interaction. At lower rotational speeds, the turbine does not fully extract the available tangential momentum of the vortex, whereas at higher rotational speeds, excessive blade–flow interaction increases turbulence and disturbs the vortex core, leading to enhanced energy dissipation. Aa around 80 RPM, the vortex structure remains stable while the blades extract angular momentum efficiently, resulting in maximum power conversion.

Figure 25 further shows that for three types of turbine blades, the turbine systems with a discharge orifice diameter of 0.16 m perform significantly better than those with $d_o = 0.14$ m and $d_o = 0.20$ m across all rotational speeds considered. In general, the performances of the turbine systems with $d_o = 0.14$ m and $d_o = 0.20$ m are very comparable. These results clearly illustrate the significant but non-monotonic effect of the discharge orifice diameter on the turbine system performance, which is also in agreement with the qualitative results as described above.

Although the maximum efficiency obtained in this study (58–62%) is higher than the typical range of 25.7–42.1% reported in previous reviews, direct comparison is not straightforward due to differences in turbine geometry, basin configuration, and numerical methodology. Only a limited number of studies consider purely cylindrical basins with runner dimensions comparable to the present design, while many include additional features such as baffles, guide vanes, or conical basins, which alter the vortex structure

and energy dissipation. In gravitational water vortex turbines, torque generation is mainly governed by the pressure gradients and tangential momentum of the rotating vortex rather than solely by the inlet kinetic energy. In addition, the steady-state MRF formulation used here provides an upper-bound estimate of performance, as unsteady losses associated with vortex breakdown and blade–vortex interaction are not resolved. These factors explain why the present efficiencies fall at the upper end of the range reported in the literature.

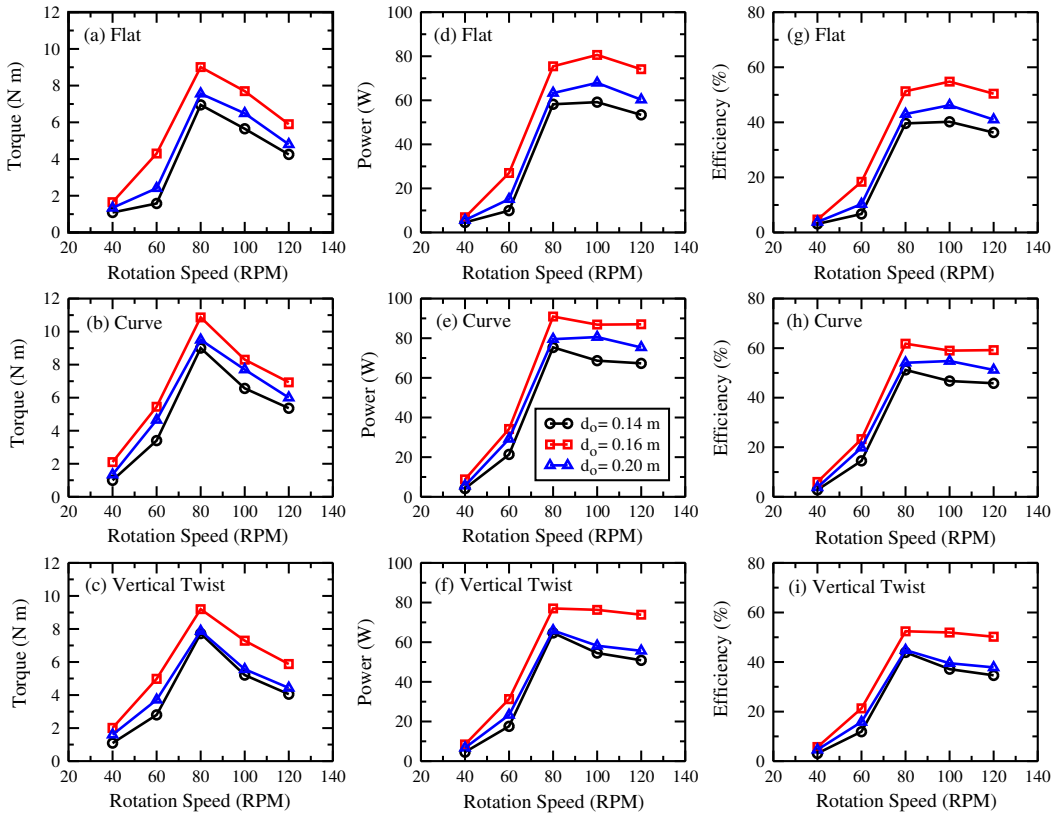

Figure 25. Torque, power, and efficiency plotted against rotation speed with different discharge orifice diameters for the three types of turbine blade: flat blades (top row), curved blades (middle row), and vertical twisted blades (bottom row).

Figure 26 reveals that for all three discharge orifice diameters considered, the turbine systems with the curve blades perform significantly better than those with the flat and vertical twisted blades across all rotational speeds considered. In general, the performances of the turbine systems with the flat and vertical twisted blades are very comparable. These results illustrate the significant effect of turbine blade shape on the turbine system performance, which is again in agreement with the qualitative results as described previously.

3.2.2. Volume-Averaged Turbulent Kinetic Energy

As turbulent kinetic energy is closely related to the power produced by a turbine, as shown above, it is worth examining its quantitative variations when the rotation speed, turbine blade shape, and discharge orifice diameter change. In Figures 27 and 28, the obtained volume-averaged turbulent kinetic energy is plotted against rotation speed for the variations in the discharge orifice diameter and blade shape. Although the data presented in these two figures are the same, similar to that for torque, power, and efficiency as shown above, such a repetition is beneficial as the individual effect of the blade shape and discharge orifice diameter can be more explicitly and separately observed from Figures 27 and Figure 28, respectively.

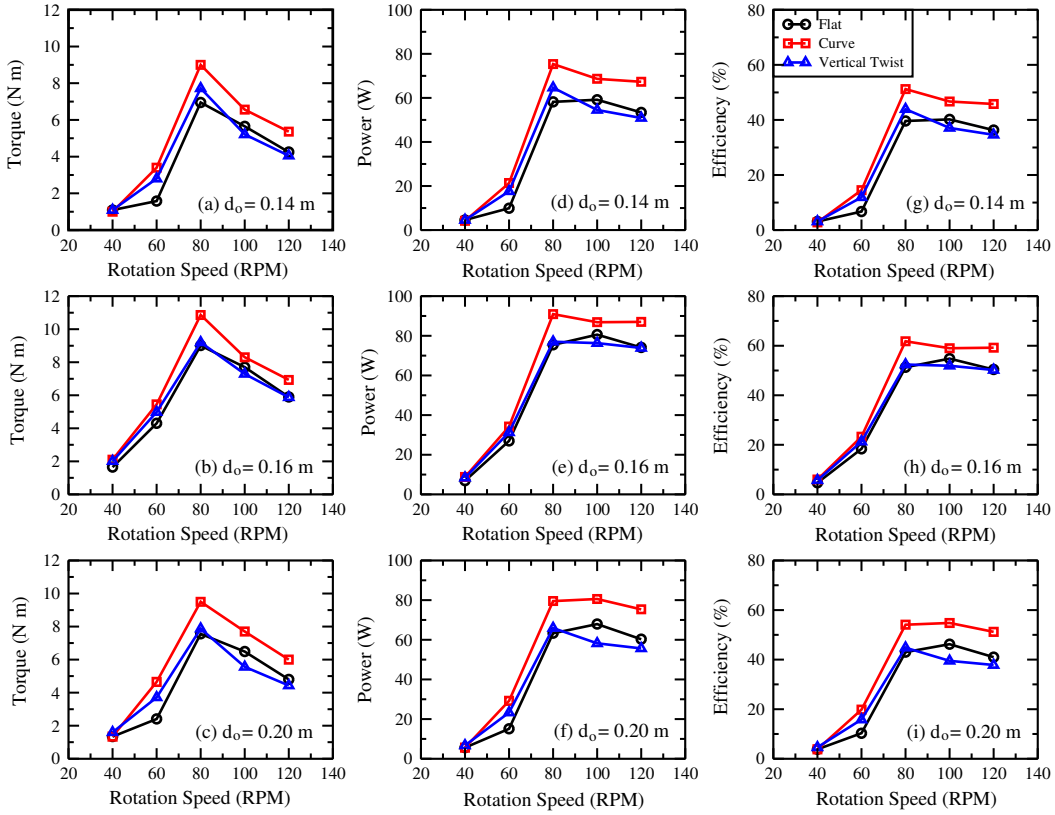

Figure 26. Torque, power, and efficiency plotted against rotation speed for the three types of turbine blades with different discharge orifice diameters: $d_o = 0.14$ m (top row), $d_o = 0.16$ m (middle row), and $d_o = 0.20$ m (bottom row).

From the results presented in the figures, it is clearly seen that the volume-averaged k is closely related to torque and power, with similar trends observed. In the numerical simulations of vortex hydropower systems with the MRF scheme, most of the volume-averaged turbulent kinetic energy is generated in the turbine region where the relative motion between blades and water is the highest [76]. It can be seen in Figure 27 that the turbine with curved blades produces larger volume-averaged k values as it produces stronger shear and more complex wake structures, leading to larger volume-averaged k in the rotating region, compared to flat or vertical twisted blades. This explains why the volume-averaged k across the rotation speeds shown in Figure 27 have larger magnitudes and earlier peaks for curved blades [77]. The flat and twisted blades produce slightly moderate volume-averaged k as they are unable to capture adequate angular momentum to generate more torque. Beyond the optimal rotation speed of 80 RPM, the volume-averaged k decreases as rotation speed increases, becomes more dissipative, and may result in a drop in torque as well [76].

From Figure 28, it can be seen that the turbine with curved blades when $d_o = 0.16$ m produces larger volume-averaged k. This is consistent with the previous findings that for gravitational vortex turbines, an optimal ratio of the discharge orifice diameter to the basin diameter (d_o/D) typically exists between 0.14 and 0.18, where power extraction and vortex stability reach peaks [78]. The stronger and more coherent vortices elevate the turbulent energy field, especially near the turbine's working height [7]. The cases with $d_o = 0.14$ m and $d_o = 0.20$ m show slightly small volume-averaged k, indicating that smaller d_o increases contractual losses, and larger d_o weakens the rotational core and results in reduced volume-averaged k and torque [78].

The existence of an optimal rotational speed indicates that turbine performance is governed by a competition between energy extraction and flow disturbance. A stable

free-surface vortex with a well-developed pressure depression is essential for the efficient operation of GWVHT systems. Excessively low rotational speeds underutilize the available vortex energy, while excessively high speeds disrupt the vortex structure through increased turbulence production and blade-induced flow separation. The optimal speed therefore corresponds to a regime where vortex stability and blade loading are simultaneously maximized.

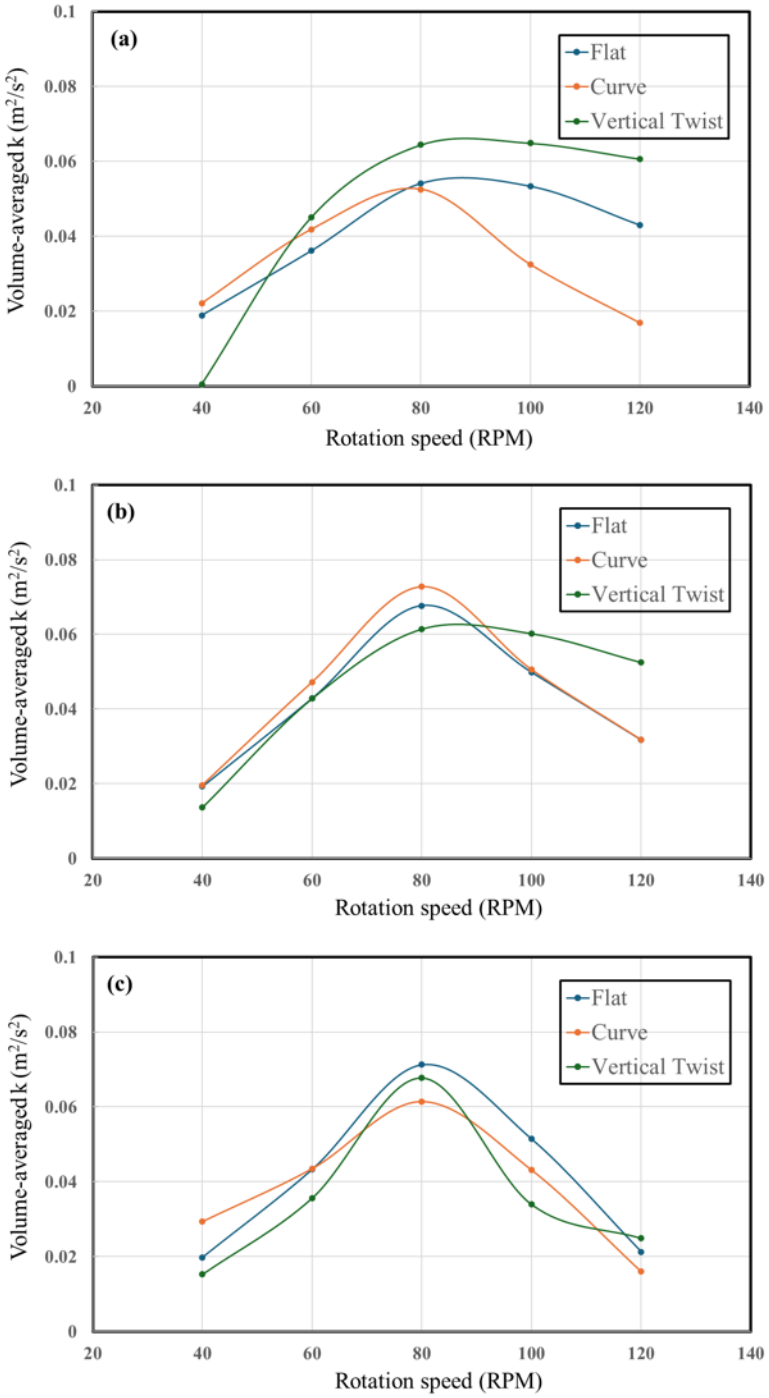

Figure 27. Volume-averaged turbulent kinetic energy k (m^2/s^2) in the whole domain plotted against rotational speed (RPM) for the three types of blade shapes at discharge diameters of 0.14 m, 0.16 m, and 0.20 m, respectively: (**a**) flat blades, (**b**) curved blades, and (**c**) vertical twisted blades.

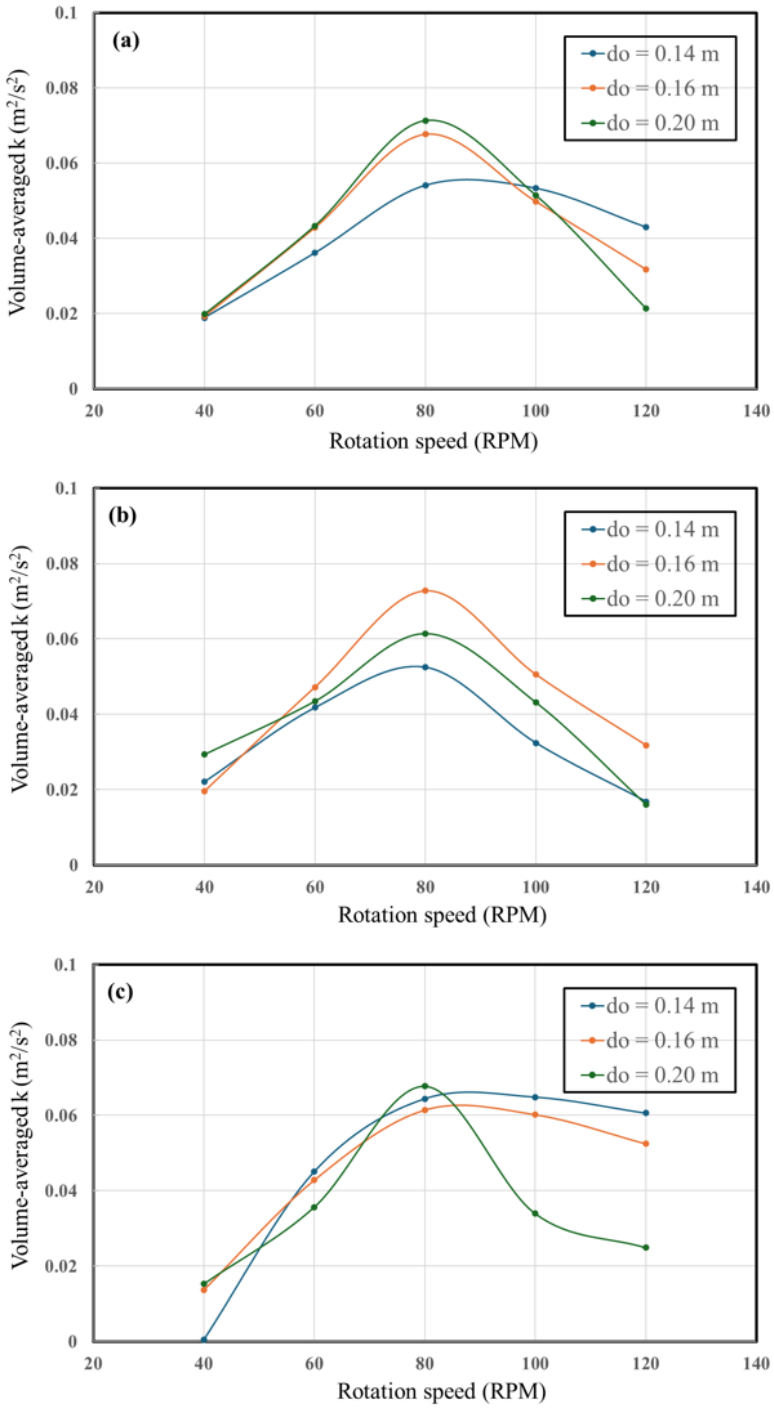

Figure 28. Volume-average turbulent kinetic energy k (m^2/s^2) in the whole domain plotted against rotational speed (RPM) for the three types of blade shapes at discharge diameters of 0.14 m, 0.16 m, and 0.20 m, respectively: (**a**) $d_o = 0.14$ m, (**b**) $d_o = 0.16$ m, and (**c**) $d_o = 0.20$ m.

4. Conclusions

A gravitational water vortex power system is one of the cost effective systems of extracting low head hydropower. In the present study, a gravitational water vortex power system, which consists of an inlet water channel, an outlet water channel, a cylindrical basin with a discharge orifice on its bottom for the discharge of water in the basin to the outlet channel, and a turbine with five blades and a vertical shaft connected to the electricity generator, was investigated numerically to examine its power generation performance. The VOF, MRF, and SST $k-\omega$ turbulence model were used in the numerical simulations.

The numerical simulations adopted a scaled down model (with a length scale factor of 1:5) using the Froude number similarity, corresponding to a typical low head of 2.5 m (available power of 41 kW) in practical applications. Three different blade shapes (flat, curved, and vertical twist) with three different discharge orifice diameters (0.14 m, 0.16 m, 0.20 m, corresponding to the ratios of the orifice diameter to the basin diameter of 0.14, 0.16, and 0.20) operated at turbine rotation speeds of 40 RPM, 60 RPM, 80 RPM, 100 RPM, and 120 RPM were studied.

The study showed that generally no air is present in the bottom basin region, which is about the bottom 2/3 of the basin containing the turbine, while the top 1/3 region is essentially occupied by air, with a noticeable mixing layer separating the air and the water regions, which varies significantly for different blade shapes, orifice diameters, and rotation speeds. The results also show that the pressure distributions at different vertical and horizontal planes vary significantly and the variations on each plane are also very substantial, particularly in the regions around the turbine and near the bottom, and three distinct regions along the vertical direction (a top region, a middle region in which its bottom boundary is just above the top of the blades, and a bottom region, which contains the turbine), with clear boundaries to separate each other, can be identified. The influences of the blade, orifice diameter, and rotation speed on the pressure distributions are also notable and the corresponding velocity and turbulent kinetic energy distributions follow similar trends, with turbulence occurring mainly in the areas around the turbine with the strongest turbulence occurring at the tips of the blades, around the discharge orifice, and at the entry location of the water in the inlet passage channel into the basin. For the majority of the remaining regions in the basin, turbulent kinetic energy is negligible, indicating that the flow is essentially laminar and in a manner of rigid-body rotation of fluid. The velocity and turbulent kinetic energy distributions were found to be significantly affected by blade shape, orifice diameter, and rotation speed change as well.

The study further shows that for each design of the hydropower system with specific blade shapes and discharge orifice diameter, the generated torque, thus power, increases almost linearly at a large rate when the rotation speed is increased from 40 RPM to 80 RPM and then decreases, also essentially linearly, at a much smaller rate when the rotation speed is further increased from 80 RPM to 120 RPM, illustrating the significant but non-monotonic effect of rotation speed on system performance. Such trends are in line with the previous studies, i.e., torque stalls after certain rotation speed whilst turbulence increases, thus highlighting the inefficiency of high speeds, and beyond stalled torque, the energy derived from increased turbulence is dissipated into the small eddies instead of useful rotation. The results indicate that for the cases considered, a relative high maximum efficiency (between 40% and 62%) can be achieved, which is a very good outcome for such low head gravitational water vortex hydro-turbine systems, and the combination of curved turbine blades, a medium discharge orifice diameter ($d_o/D \approx 0.16$), and a rotational speed of 80 RPM provides the most favorable operating condition, yielding the highest efficiency and torque among all configurations considered.The high achievement is a result of the pressure dominated torque and blade radius effects, which govern the upper bound torque of performance in the low head cylindrical vortex turbines, particularly under the MRF steady state modeling. Furthermore, the study revealed that, across all rotation speeds considered, for each blade shape, the systems with the orifice diameter of 0.16 m perform better than those with 0.14 m and 0.20 m, while for each orifice diameter, the turbine system with the curved blades performs better than those with the flat and vertical twisted blades. In addition, the results demonstrate that the volume-averaged k in the domain is closely and quantitatively related to torque and power, with similar trends observed, which provides some insights into the mechanisms involved.

From a practical design perspective, the present results suggest that a GWVHT system employing curved blades, a discharge orifice diameter ratio of approximately 0.16, and a rotational speed close to 80 RPM can be considered as a reference configuration for efficient operation under ultra-low-head conditions. This configuration offers an optimal balance between vortex stability, effective angular momentum extraction, and controlled turbulence generation, making it suitable for prototype development and field implementation.

Author Contributions: Conceptualization, N.M., M.K., and W.L.; methodology, N.M. and W.L.; formal analysis, N.M. and W.L.; investigation, N.M. and W.L.; resources, W.L. and M.K.; data curation, N.M. and W.L.; writing—original draft preparation, N.M. and W.L.; supervision, W.L. and M.K. All authors have read and agreed to the published version of the manuscript.

Funding: This research received no external funding.

Data Availability Statement: The data presented in this study are available on request from the corresponding author.

Conflicts of Interest: The authors declare no conflicts of interest.

References

1. International Hydropower Association. *2024 World Hydropower Outlook—Opportunities to Advance Net Zero*; International Hydropower Association: London, UK, 2024.
2. The United Nations Industrial Development Organization and the International Center on Small Hydro Power. The World Small Hydropower Development Report 2022. 2022. Available online: https://www.unido.org/WSHPDR2022 (accessed on 15 November 2024).
3. Zotloterer, F. Gravitational Water Vortex Power Plants. 2004. Available online: http://www.zotloeterer.com/welcome/gravitation-water-vortex-power-plants/reference-plants/ (accessed on 15 November 2024).
4. Timilsina, A.B.; Mulligan, S.; Bajracharya, T.R. Water vortex hydropower technology: A state-of-the-art review of developmental trends. *Clean Technol. Environ. Policy* **2018**, *20*, 1737–1760. [CrossRef]
5. Chen, H.X.; Shi, F.J.; Guo, J.H. Numerical research on the three dimensional unsteady flow within the vortex pump. *Int. J. Turbo Jet-Engines* **2006**, *23*, 27–36. [CrossRef]
6. Li, H.; Chen, H.; Ma, Z.; Zhou, Y. Formation and Influencing Factors of Free Surface Vortex in a Barrel with a Central Orifice at Bottom. *J. Hydrodyn. Ser. B* **2009**, *21*, 238–244. [CrossRef]
7. Maika, N.; Lin, W.; Khatamifar, M. A review of gravitational water vortex hydro turbine systems for hydropower generation. *Energies* **2023**, *16*, 5394. [CrossRef]
8. Velásquez, L.; Rengifo, J.P.; Urrego, J.; Rubio-Clemente, A.; Chica, E. Experimental Assessment of Hydrodynamic Behavior in a Gravitational Vortex Turbine with Different Inlet Channel and Discharge Basin Configurations. *Energies* **2024**, *17*, 5773. [CrossRef]
9. Sinagra, M.; Picone, C.; Picone, P.; Aricò, C.; Tucciarelli, T.; Ramos, H.M. Low-head hydropower for energy recovery in wastewater systems. *Water* **2022**, *14*, 1649. [CrossRef]
10. Picone, C.; Sinagra, M.; Gurnari, L.; Tucciarelli, T.; Filianoti, P.G. A new cross-flow type turbine for ultra-low head in streams and channels. *Water* **2023**, *15*, 973. [CrossRef]
11. Ham, S.; Adeeb, E.; Lee, J.W.; Ha, H. Numerical evaluation of low-head inverted cross-flow turbine design method: A comprehensive study. *Energy Convers. Manag.* **2024**, *311*, 118521. [CrossRef]
12. Picone, C.; Sinagra, M.; Tucciarelli, T. A new regulation system for Crossflow type turbines for water management industry. *Energy* **2025**, *328*, 136695. [CrossRef]
13. Malek, A.; Shehata, A.S.; Elsherbiny, K.; Mehanna, A. CFD analysis of a gravitational whirlpool hydropower turbine at Egyptian riverine system. *AIP Conf. Proc.* **2023**, *2769*, 020020. [CrossRef]
14. Mamadjanov, A.; Yusupov, D.; Berkinov, E.; Akmalov, J.; Jalilov, M. The effect of conical basin geometry on gravitational water vortex power plant. In *E3S Web of Conferences*; EDP Sciences: Les Ulis, France, 2024; Volume 563, p. 01010.
15. Velásquez, L.; Posada, A.; Chica, E. Surrogate modeling method for multi-objective optimization of the inlet channel and the basin of a gravitational water vortex hydraulic turbine. *Appl. Energy* **2023**, *330*, 120357. [CrossRef]
16. Premaratne, P.; Kadhim, I.J.; Abdullah, M.Q.; Halloran, B.; Vial, P.J. A survey on low speed low power axial flux generator performance and design considerations. *Neurocomputing* **2022**, *509*, 272–289. [CrossRef]
17. Di Dio, V.; Cipriani, G.; Manno, D. Axial flux permanent magnet synchronous generators for pico hydropower application: A parametrical study. *Energies* **2022**, *15*, 6893. [CrossRef]

18. Thapa, B.S.; Dahlhaug, O.G.; Thapa, B. Sediment erosion in hydro turbines and its effect on the flow around guide vanes of Francis turbine. *Renew. Sustain. Energy Rev.* **2015**, *49*, 1100–1113. [CrossRef]
19. Rahman, M.M.; Tan, J.H.; Fadzlita, M.T.; Muzammil, A.R.W.K. A review on the development of gravitational water vortex power plant as alternative renewable energy resources. *IOP Conf. Ser. Mater. Sci. Eng.* **2017**, *217*, 12007. [CrossRef]
20. Sierra, J.; Ruiz, A.; Guevara, A.; Posada, A. Review: Gravitational vortex turbines as a renewable energy. *Int. J. Fluid Mach. Syst.* **2020**, *13*, 704–717. [CrossRef]
21. Velásquez, L.; Chica, E.; Posada, J. Advances in the development of gravitational water vortex hydraulic turbines. *J. Eng. Sci. Technol. Rev.* **2021**, *14*, 1–14. [CrossRef]
22. Wanchat, S.; Suntivarakorn, R.; Wanchat, S.; Tonmit, K.; Kayanyiem, P. A Parametric study of a gravitation vortex power plant. *Adv. Mater. Res.* **2013**, *805–806*, 811–817. [CrossRef]
23. Ullah, R.; Cheema, T.A.; Saleem, A.S.; Ahmad, S.M.; Chattha, J.A.; Park, C.W. Performance analysis of multi-stage gravitational water vortex turbine. *Energy Convers. Manag.* **2019**, *198*, 111788. [CrossRef]
24. Wang, Y.; Jiang, C.; Chen, Z. Experimental research on vertical vortex in spillway tunnel intake. *Shui Li Fa Dian Xue Bao* **2010**, *29*, 21–25.
25. Anh, T.N.; Hosoda, T. Depth-averaged model of open-channel flows over an arbitrary 3D surface and its applications to analysis of water surface profile. *J. Hydraul. Eng.* **2007**, *133*, 350–360. [CrossRef]
26. Mulligan, S.; Creedon, L.; Casserly, J.; Sherlock, R. An improved model for the tangential velocity distribution in strong free-surface vortices: An experimental and theoretical study. *J. Hydraul. Res.* **2019**, *57*, 547–560. [CrossRef]
27. Mulligan, S.; Casserly, J.; Sherlock, R. Effects of geometry on strong free-surface vortices in subcritical approach flows. *J. Hydraul. Eng.* **2016**, *142*, 04016051. [CrossRef]
28. Velásquez García, L.; Rubio-Clemente, A.; Chica, E. Runner optimal position in a gravitational water vortex hydraulic turbine with a spiral inlet channel and a conical basin. *Renew. Energy Power Qual. J.* **2022**, *20*, 143–147. [CrossRef]
29. Edirisinghe, D.S.; Yang, H.S.; Kim, B.H.; Kim, C.G.; Gunawardane, S.D.G.S.P.; Lee, Y.H. Numerical optimization of gravitational water vortex turbine using computational flow analysis. *IOP Conf. Ser. Earth Environ. Sci.* **2022**, *1037*, 12004. [CrossRef]
30. Edirisinghe, D.S.; Yang, H.; Gunawardane, S.D.G.S.P.; Lee, Y. Enhancing the performance of gravitational water vortex turbine by flow simulation analysis. *Renew. Energy* **2022**, *194*, 163–180. [CrossRef]
31. Velásquez, L.; Romero-Menco, F.; Rubio-Clemente, A.; Posada, A.; Chica, E. Numerical optimization and experimental validation of the runner of a gravitational water vortex hydraulic turbine with a spiral inlet channel and a conical basin. *Renew. Energy* **2024**, *220*, 119676. [CrossRef]
32. Varga, M.; Velásquez1, L.; Rubio-Clemente1, A.; Valencia, B.R.; Chica, E. Experimental analysis of Gravitational Vortex Turbine made from natural fibers. *Materials* **2025**, *18*, 2352. [CrossRef]
33. Garcia, M.D.; Montoya, J.A.P.; Chica, E.; Montoya, J.F.H.; Velásquez, L.; Arcila, I.D.P. A comprehensive assessment of the applicability of semianalytical models of vortex characterization for gravitational water vortex hydropower plants. *Sci. Rep.* **2025**, *15*, 37671. [CrossRef]
34. Ullah, R.; Cheema, T.A.; Saleem, A.S.; Ahmad, S.M.; Chattha, J.A.; Park, C.W. Preliminary experimental study on multi-stage gravitational water vortex turbine in a conical basin. *Renew. Energy* **2020**, *145*, 2516–2529. [CrossRef]
35. Ruiz Sánchez, A.; Guevara MuÑOz, A.; Sierra Del Rio, J.A.; Posada Montoya, J.A. Numerical comparison of two runners for gravitational vortex turbine. *Eng. Trans.* **2021**, *69*, 3–17.
36. Kim, M.S.; Edirisinghe, D.S.; Yang, H.S.; Gunawardane, S.D.G.S.P.; Lee, Y.H. Effects of blade number and draft tube in gravitational water vortex power plant determined using computational fluid dynamics simulations. *J. Adv. Mar. Eng. Technol.* **2021**, *45*, 252–262. [CrossRef]
37. Nishi, Y.; Sukemori, D.; Inagaki, T. Performance and flow field of gravitation vortex type water turbine using volute tank. *Int. J. Fluid Mach. Syst.* **2021**, *14*, 229–246. [CrossRef]
38. Nishi, Y.; Inagaki, T. Performance and flow field of a gravitation vortex type water turbine. *Int. J. Rotating Mach.* **2017**, *2017*, 2610508. [CrossRef]
39. Nishi, Y.; Suzuo, R.; Sukemori, D.; Inagaki, T. Loss analysis of gravitation vortex type water turbine and influence of flow rate on the turbine's performance. *Renew. Energy* **2020**, *155*, 1103–1117. [CrossRef]
40. Edirisinghe, D.S.; Yang, H.; Gunawardane, S.D.G.S.P.; Alkhabbaz, A.; Tongphong, W.; Yoon, M.; Lee, Y. Numerical and experimental investigation on water vortex power plant to recover the energy from industrial wastewater. *Renew. Energy* **2023**, *204*, 617–634. [CrossRef]
41. Mulligan, S.; De Cesare, G.; Casserly, J.; Sherlock, R. Understanding turbulent free-surface vortex flows using a Taylor-Couette flow analogy. *Sci. Rep.* **2018**, *8*, 824. [CrossRef]
42. Gupta, A.; Prakash, A.; Singh, G.K.; Tripathi, H. Design of a micro hydro power plant based on the vortex flow of water. *Int. J. Adv. Res. Sci. Commun. Technol.* **2021**, *5*, 420–427. [CrossRef]

43. Velásquez, L.; Rubio-Clemente, A.; Chica, E. Numerical and experimental analysis of vortex profiles in gravitational water vortex hydraulic turbines. *Energies* **2024**, *17*, 3543. [CrossRef]
44. Vinayakumar, B.; Antony, R.; Binson, V.; Youhan, S. Experimental and numerical study on gravitational water vortex power plant for small water bodies. *E-Prime Electr. Eng. Electron. Energy* **2024**, *7*, 100460. [CrossRef]
45. Akhyar, A.; Sofyan, S.E. A review of vortex water turbine design for sustainable energy generation (principles, optimization, and validation). *Energy Convers. Manag. X* **2025**, *26*, 100895. [CrossRef]
46. Dhakal, R.; Bajracharya, T.R.; Shakya, S.R.; Kumal, B.; Khanal, K.; Williamson, S.J.; Gautam, S.; Ghale, D.P. Computational and experimental investigation of runner for gravitational water vortex power plant. In Proceedings of the 2017 IEEE 6th International Conference on Renewable Energy Research and Applications (ICRERA 2017), San Diego, CA, USA, 5–8 November 2017; pp. 365–373.
47. Hirt, C.W.; Nichols, B.D. Volume of fluid (VOF) method for the dynamics of free boundaries. *J. Comp. Phys.* **1981**, *39*, 201–225. [CrossRef]
48. Velásquez, L.; Posada, A.; Chica, E. Optimization of the basin and inlet channel of a gravitational water vortex hydraulic turbine using the response surface methodology. *Renew. Energy* **2022**, *187*, 508–521. [CrossRef]
49. Powalla, D.; Hoerner, S.; Cleynen, O.; Müller, N.; Stamm, J.; Thévenin, D. A computational fluid dynamics model for a Water vortex power plant as platform for etho- and ecohydraulic research. *Energies* **2021**, *14*, 639. [CrossRef]
50. Zamora-Juárez, M.A.; Guerra-Cobián, V.H.; Ortiz, C.R.F.; López-Rebollar, B.M.; Fierro1, A.L.F.; Flores, J.L.B. Performance of modified gravitational water vortex turbine through CFD for hydro power generation on micro-scale. *J. Braz. Soc. Mech. Sci. Eng.* **2022**, *44*, 545. [CrossRef]
51. Pamuji, D.S.; Effendi, N.; Sugati, D. Numerical study on the performance and flow field of varied conical basin for efficient gravitational water vortex power plant. In *AIP Conference Proceedings*; AIP Publishing LLC: Melville, NY, USA, 2019; Volume 2187, p. 020001.
52. Eltayesh, A.; Castellani, F.; Burlando, M.; Hanna, M.B.; Huzayyin, A.S.; El-Batsh, H.M.; Becchetti, M. Experimental and numerical investigation of the effect of blade number on the aerodynamic performance of a small-scale horizontal axis wind turbine. *Alex. Eng. J.* **2021**, *60*, 3931–3944. [CrossRef]
53. Kim, K.; Kim, D.; Hong, S.; Lee, S. Computational Fluid Dynamics Analysis and Validation with Field Test of 1 MW Hydropower Turbine System. *Energies* **2025**, *18*, 628. [CrossRef]
54. Nigussie, T.; Engeda, A.; Dribssa, E. Design, Modeling, and CFD Analysis of a Micro Hydro Pelton Turbine Runner: For the Case of Selected Site in Ethiopia. *Int. J. Rotating Mach.* **2017**, *2017*, 3030217. [CrossRef]
55. Nishi, Y.; Inagaki, T.; Li, Y.; Hatano, K. Study on an Undershot Cross-Flow Water Turbine with Straight Blades. *Int. J. Rotating Mach.* **2015**, *2015*, 817926. [CrossRef]
56. Yosry, A.G.; Álvarez, E.A.; Valdés, R.E.; Pandal, A.; Marigorta, E.B. Experimental and multiphase modeling of small vertical-axis hydrokinetic turbine with free-surface variations. *Renew. Energy* **2023**, *203*, 788–801. [CrossRef]
57. ANSYS, Inc. Flows with Moving and Rotating Objects, 2020. Available online: https://innovationspace.ansys.com/courses/wp-content/uploads/2020/09/Flows-with-Moving-and-Rotating-Objects-Lesson-4-Handouts-1.pdf (accessed on 12 March 2025).
58. Eltayesh, A.; Hanna, M.B.; Castellani, F.; Huzayyin, A.S.; El-Batsh, H.M.; Burlando, M.; Becchetti, M. Effect of Wind Tunnel Blockage on the Performance of a Horizontal Axis Wind Turbine with Different Blade Number. *Energies* **2019**, *12*, 1988. [CrossRef]
59. Franzke, R.; Sebben, S.; Bark, T.; Willeson, E.; Broniewicz, A. Evaluation of the Multiple Reference Frame Approach for the Modelling of an Axial Cooling Fan. *Energies* **2019**, *12*, 2934. [CrossRef]
60. Liu, J.; Lin, H.; Purimitla, S.R. Wake field studies of tidal current turbines with different numerical methods. *Ocean Eng.* **2016**, *117*, 383–397. [CrossRef]
61. Cano-Perea, G.; Mendoza, E.; López-Rebollar, B.M. Numerical analysis of a ducted water current turbine for low energetic flow conditions. *J. Ocean Eng. Mar. Energy* **2024**, *10*, 217–237. [CrossRef]
62. Silva, P.A.S.F.; Tsoutsanis, P.; Antoniadis, A.F. Simple multiple reference frame for high-order solution of hovering rotors with and without ground effect. *Aerosp. Sci. Technol.* **2021**, *111*, 106518. [CrossRef]
63. ANSYS, Inc. *Ansys Fluent Theory Guide*; ANSYS, Inc.: Canonsburg, PA, USA, 2021.
64. Faraji, A.; Jande, Y.A.C.; Kivevele, T. Performance analysis of a runner for gravitational water vortex power plant. *Energy Sci. Eng.* **2022**, *10*, 1055–1066. [CrossRef]
65. Haghighi, M.H.S.; Mirghavami, S.M.; Chini, S.F.; Riasi, A. Developing a method to design and simulation of a very low head axial turbine with adjustable rotor blades. *Renew. Energy* **2019**, *135*, 266–276. [CrossRef]
66. Bajracharya, T.R.; Shakya, S.R.; Timilsina, A.B.; Dhakal, J.; Neupane, S.; Gautam, A.; Sapkota, A. Effects of geometrical parameters in gravitational water vortex turbines with conical basin. *J. Renew. Energy* **2020**, *2020*, 5373784. [CrossRef]
67. Mukherji, S.S. Design and Critical Performance Evaluation of Horizontal Axis Hydrokinetic Turbines. Master's Thesis, Missouri University of Science and Technology, Rolla, MO, USA, 2010.

68. Carcangiu, C.E. CFD-RANS Study of Horizontal Axis Wind Turbines. Ph.D. Thesis, Università degli Studi di Cagliari, Cagliari, Italy, 2008.
69. Abutunis, A.; Fal, M.; Fashanu, O.; Chandrashekhara, K.; Duan, L. Coaxial horizontal axis hydrokinetic turbine system: Numerical modeling and performance optimization. *J. Renew. Sustain. Energy* **2021**, *13*, 024502. [CrossRef]
70. Khedr, A.; Castellani, F. Critical issues in the moving reference frame CFD simulation of small horizontal axis wind turbines. *Energy Convers. Manag. X* **2024**, *22*, 100551. [CrossRef]
71. Tian, W.; Song, B.; VanZwieten, J.H.; Pyakurel, P.; Li, Y. Numerical simulations of a horizontal axis water turbine designed for underwater mooring platforms. *Int. J. Nav. Archit. Ocean Eng.* **2016**, *8*, 73–82. [CrossRef]
72. ANSYS, Inc. ANSYS Fluent Mosaic Technology Automatically Combines Disparate Meshes with Polyhedral Elements for Fast, Accurate Flow Resolution. 2020. Available online: https://www.ansys.com/content/dam/resource-center/white-paper/ansys-fluent-mosaic-technology-wp.pdf (accessed on 12 March 2025).
73. Zore, K.; Caridi, D.; Lockley, I. Fast and Accurate Prediction of Vehicle Aerodynamics Using ANSYS Mosaic Mesh, SAE Technical Paper 2020-01-5011, ANSYS Inc. 2020. Available online: https://www.sae.org/publications/technical-papers/content/2020-01-5011/ (accessed on 12 March 2025).
74. Sukadana, I.G.K.; Suarda, M.; Widiarta, I.P.; Danus, I. CFD (Computational Fluid Dynamics) Simulation of Hydrodynamic Vortex Turbine Performance: Influence of Notch Angle Variation on Flow Patterns and Efficiency. *Nat. Sci. Eng. Technol. J.* **2024**, *4*, 336–351. [CrossRef]
75. Dhakal, S.; Timilsina, A.B.; Dhakal, R.; Fuyal, D.; Bajracharya, T.R.; Pandit, H.P.; Amatya, N.; Nakarmi, A.M. Comparison of cylindrical and conical basins with optimum position of runner: Gravitational water vortex power plant. *Renew. Sustain. Energy Rev.* **2015**, *48*, 662–669. [CrossRef]
76. Gorgun, E. Numerical analysis of inflow turbulence intensity impact on the stress and fatigue life of vertical axis hydrokinetic turbine. *Phys. Fluids* **2024**, *36*, 015111. [CrossRef]
77. Shen, C.; Han, Y.; Wang, S.; Wang, Z. Influence of Airfoil Curvature and Blade Angle on Vertical Axis Hydraulic Turbine Performance in Low Flow Conditions. *Water* **2024**, *17*, 11. [CrossRef]
78. Sreerag, S.R.; Raveendran, C.K.; Jinshah, B.S. Effect of outlet diameter on the performance of gravitational vortex turbine with conical basin. *Int. J. Sci. Eng. Res.* **2016**, *7*, 457–463.